Spanning spatial scales with functional imaging in the human brain at 10.5 Tesla

Luca Vizioli[1*], Lasse Knudsen[1], Steen Moeller[1], Logan Dowdle[2], Andrea Grant[1], Alireza Sadeghi-Tarakameh[1], Yulia Lazarova[1], Nils Nothnagel[1], Yigitcan Eryaman[1], Matt Waks[1], Russel L. Lagore[1], Edward Auerbach[1], Gregor Adriany[1], Federico De Martino[2], Lonike Faes[2], Essa Yacoub[1], Kamil Uğurbil[1]

1. Center for Magnetic Resonance Research (CMRR), University of Minnesota, Minneapolis, MN 55455

2. Department of Cognitive Neuroscience, Maastricht University, Maastricht, Universiteitssingel 40, 6229 ER Maastricht, Netherlands

*Corresponding author
lvizioli@umn.edu
luca.vizioli1@gmail.com

ABSTRACT

One of the most important frontiers in the efforts to improve functional imaging of brain activity (fMRI) is the recent push to increase the magnetic fields for human imaging beyond 10 Tesla. Having established safety, large gains in signal-to-noise-ratio (SNR), and novel radiofrequency arrays that capture the higher SNR, here we demonstrate major gains in the spatial resolution, sensitivity, and functional contrast of BOLD (Blood Oxygenation Level Dependent) based human fMRI at 10.5 Tesla. Using image reconstruction methods developed to minimize blurring, we also demonstrate that ultrahigh resolutions achieved at 10.5 Tesla suppress large-vein confounds in gradient-recalled-echo BOLD fMRI, thus improving the fidelity of functional signals relative to neuronal activity and yielding accurate cortical depth-profiles for layer-specific activation. Together, these multiplicative benefits deliver much needed increases in precision and resolution for meso-scale fMRI applications and illustrate the transformative potential of human functional imaging at magnetic fields that exceed 10 Tesla.

1. INTRODUCTION

Following its introduction[1,2], functional MRI (fMRI) based on the Blood Oxygen Level Dependent (BOLD) contrast has rapidly emerged as the most widely used noninvasive tool employed for human brain studies. Nevertheless, like all techniques at our disposal for studying the brain, fMRI has limitations, particularly with respect to spatiotemporal resolution and the fidelity of the functional maps relative to the neuronal activity that induces them.

The brain operates over a vast spatial scale, going from individual cells to mesoscale neuronal ensembles and ultimately to brain-wide networks involving billions of neurons. However, at the spatial resolutions employed in the vast majority of human fMRI experiments, the fMRI voxel is $\gtrsim$8μL in volume (e.g. 2mm isotropic resolution), containing more than a million neurons. Nevertheless, given the scarcity of knowledge on human brain function, much can be learned from studies caried out at such coarse resolutions. However, despite the relatively high signal-to-noise ratio (SNR) of the image at such low resolutions, detecting the inherently small functional signals remains difficult. Addressing this challenge often requires group-level studies involving large number of subjects, and/or prolonged and repeated scanning sessions with single individuals (e.g.[3,4] references therein). Aiming for higher spatiotemporal resolutions significantly exacerbates the problem due to the consequent decreases in SNR and functional contrast-to-noise ratio (fCNR).

An additional complication arises from the indirect nature of functional signals in fMRI which reflect neuronal activity through neurovascular coupling. A well-known deleterious consequence of this indirect process is the draining-vein confound associated with gradient-recalled echo (GRE) BOLD fMRI (e.g.[5-12]), by far the most sensitive and commonly employed fMRI technique for studying the brain. This confound leads to displacement and blurring of the recorded functional maps relative to the neuronal activity that elicits them.

Overcoming the afore-listed limitations has been a major research focus since the introduction of the fMRI technique; in this effort, the development of ultrahigh magnetic fields (UHF, defined as ≥ 7 Tesla) for human imaging[13,14] has been one of, if not the most, consequential initiative. Higher magnetic fields provide increases in SNR[15-20], fCNR[14], and the relative contribution of the weak but spatially accurate functional signals associated with microvasculature (e.g.[21,22]). With these advantages, 7 Tesla (7T) fMRI ushered in the ability to break the mm-resolution barrier and access mesoscale neuronal organizations (e.g., [8,14,23-33]), starting with the demonstration of functional mapping of ocular dominance columns and orientation domains in the same individual[34]. In addition, 7T was shown to provide higher detection sensitivity and model predictive power (e.g.,[35-37]) at any spatial resolution.

Yet, robustly accessing mesoscale computations in the human brain with resolutions achievable even at 7T, typically 0.8mm isotropic (~0.5μL voxel volume), remains challenging. Such voxels still contain more than forty thousand neurons[38], capable of performing a multitude of different computations (e.g.,[39,40]). This limitation was recognized in the strategic plan developed for the US BRAIN Initiative, which codified resolution targets of ≤0.1μL voxel volume initially[41,42] and 0.01μL five years later[43], emphasizing the *"ambitious*" and *"elusive*" nature of these targets.

One of the recent major initiatives undertaken to meet these challenges is the effort to push human imaging beyond 10T[44,45], spearheaded by the 10.5T effort in our laboratory[17-20,46-50]. Having established safety[49,51], large SNR gains for human brain imaging[17-20], and novel radiofrequency arrays that capture these SNR gains[19,20], we report the first results pushing the limits of functional imaging at this unique magnetic field, demonstrating unprecedented gains in spatial resolution and precision.

2. RESULTS

All resolutions given are isotropic and, unless otherwise specified, "nominal" - which refers to the resolution indicated for the data acquisition. The *effective* voxel dimensions typically exceed

the nominal resolution but are rarely reported. In this paper, when relevant, we report estimates of functional blurring (see methods), which provide an indication of the *effective* resolution.

2.1. Quantitative T2 measurements*

T2* is a critical parameter in fMRI (e.g.[5,52]) and depends on the spatial resolution and the magnetic field used. Hence, measurements of T2* in the entire brain were performed at two different spatial resolutions and two different magnetic fields. We used Multi-Echo GRE (ME-GRE) sequence in the same subject at 10.5T to obtain whole-brain T2* measurements at 0.37- and 0.8-mm resolutions. A partial field of view acquisition (axial slab, centered around the calcarine fissure) at 0.35mm resolution was also obtained at 7T. Following processing and tissue segmentation, we obtained voxel-wise estimates of the T2* using a nonlinear fitting approach. For visualization, these fits were used to perform a weighted average of the 10.5T 0.37mm data (Figure 1a).

The distributions of gray and white matter T2* values (Figure 1b) were derived from gray and white matter segmentations in the 10.5T 0.37mm data and show high variability across the cortex. Using the gray matter segmentation, we examined the T2* as a function of depth within a region in the primary visual cortex V1. We observe a decrease in T2* (Figure 1c) at the mid-cortical depth, expected due to the presence of myelinated fibers associated with the Stria of Gennari in the middle layer of V1. This effect was also visible in the signal intensity of the weighted average images (Figure 1c, left panel).

T2* was further investigated in the primary visual cortex and the insulae, by combining gray matter segmentations with atlas-derived measures of these regions (See Methods). The 10.5T 0.37mm data (Figure 1d) showed a marked increase in T2* estimates relative to the 0.8mm data at the same field strength (Figure 1e) for both regions. In the visual cortex, gray matter T2* (median) at 10.5T were 21 vs. 18ms for 0.37- and 0.8-mm resolution data, respectively. For the insulae at 10.5T, the corresponding numbers were 31 vs. 22ms. The T2* estimates with 0.8 mm

resolution at 10.5T are similar to what is expected based on extrapolations from 9.4T data[16].

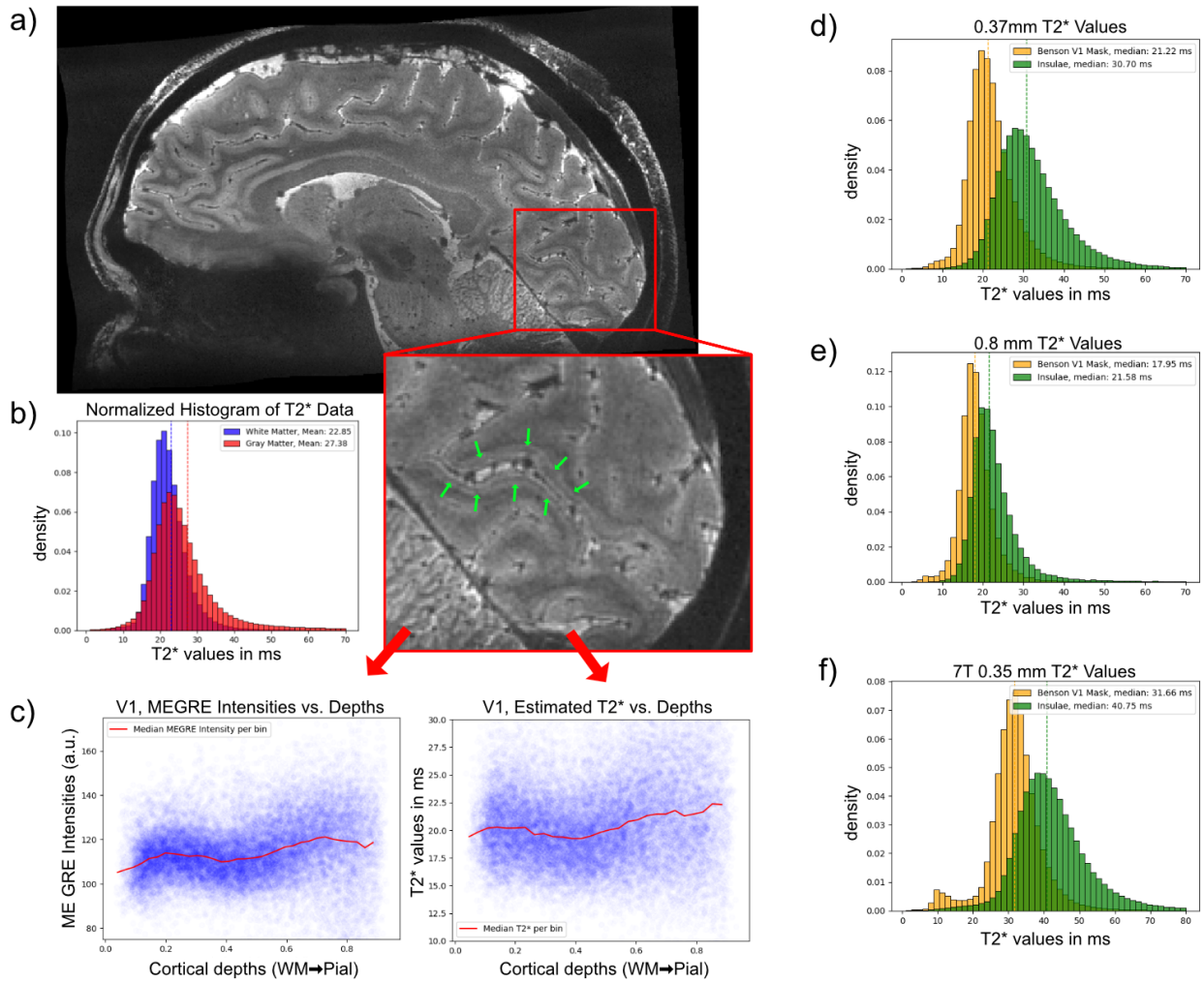

Figure 1: Quantitative T2* measurements at 10.5T obtained with ME-GRE with 0.37 mm (2 runs, 7 echoes covering 4.07 – 27.4ms) and 0.8 mm (3 runs, 7 echoes, 4 – 28ms) resolutions (panels **a** through **e**) and 7T with 0.35 mm resolution (6 runs, 6 echoes, 4.37 – 26.22) (panel **f**). **a**) average image of ME-GRE runs at 10.5T with a 0.37mm isotropic spatial resolution, zooming in on the calcarine sulcus, where the Stria of Gennari (the dark thin line indicated by the green arrows), which runs in the middle of the cortex on both the upper and lower banks of the calcarine sulcus, is clearly visible. Note that in these images, the cortex appears lighter gray compared to the white matter, and the myelinated fibers of the Stria of Gennari form a darker line in the middle of the cortex. **b)** Normalized histogram of T2* values (ms) for gray matter (red) and white matter (blue) for the 0.37mm data. Dotted vertical lines represent the medians. **c)** ME GRE intensities (left) and estimated T2* values (ms) across cortical depths. Panels **d-f** show the histograms of T2* values (ms) for V1 (in yellow) and insulae (green) for 10.5T 0.37mm data **(d)** and 0.8mm data **(e)**, and for 7T 0.35mm data **(f).** Dotted lines represent the median.

However, the 0.37mm data indicate that the magnetic fields are more homogenous over such smaller voxels, as expected. At 7T, 0.35mm acquisition yields approximately 10 ms longer T2* for both the visual cortex and insulae gray matter relative to their 10.5T counterparts with a similarly high resolution (Figure 1f), displaying the expected linear dependence of 1/T2* with the field magnitude.

2.2. 0.4 mm isotropic resolution BOLD EPI images in visual cortex at 10.5T

To evaluate the BOLD fMRI gains at 10.5T relative to 7T, we recorded 0.4mm (i.e. 0.064μL voxel) resolution functional images in two participants at 10.5T and 7T (Figure 2) using otherwise matched approaches and parameters. Acquisitions were based on 3D GRE-EPI in a slab placed over the occipital cortex. The TE was ~24 ms, which is near optimal for BOLD-fMRI at both fields, positioning the acquisition close to but on two different sides of the broad maximum defined by TE=T2*[5,52]. The experimental paradigm was that implemented in[53], consisting of a 24-second on/off block design with a center and surround flickering checkerboard stimulation, and data was acquired in consecutive ~5-min runs. Data were processed with the vendor default reconstruction *without* NORDIC.

We carried out a region of interest (ROI) analysis (see Methods) confined in the grey matter within the retinotopic representation of target and surround in V1 (Figure 2a). To avoid confounds related to SNR and BOLD response differences across fields strengths, the ROI was anatomically defined using Benson probabilistic atlas, guided by one functional run (which was excluded from further analyses - see Methods). Percent signal change (PSC) elicited by target and surround was estimated across the five remaining runs. The ROI-averaged mean PSC across trials was 6.08±0.46(SEM) and 2.83±0.29(SEM) in one subject (two-sample t-test, $t(58) = 6.00$; $p < 0.001$) and 5.11±0.34(SEM) and 2.65±0.37(SEM) in the other subject (two-sample t-test, $t(58) = 4.92$; $p < 0.001$) at 10.5T and 7T, respectively, corresponding to a supralinear increase with respect to the magnetic field strength.

Figure 2b shows the t-maps for the same t-contrast target ∩ surround > 0 for a single run (left; t>2.5) and for all 6 concatenated runs (right; t>3.5) for both field strengths and subjects superimposed on representative slices of the co-registered MP2RAGE images. In figure 2c we

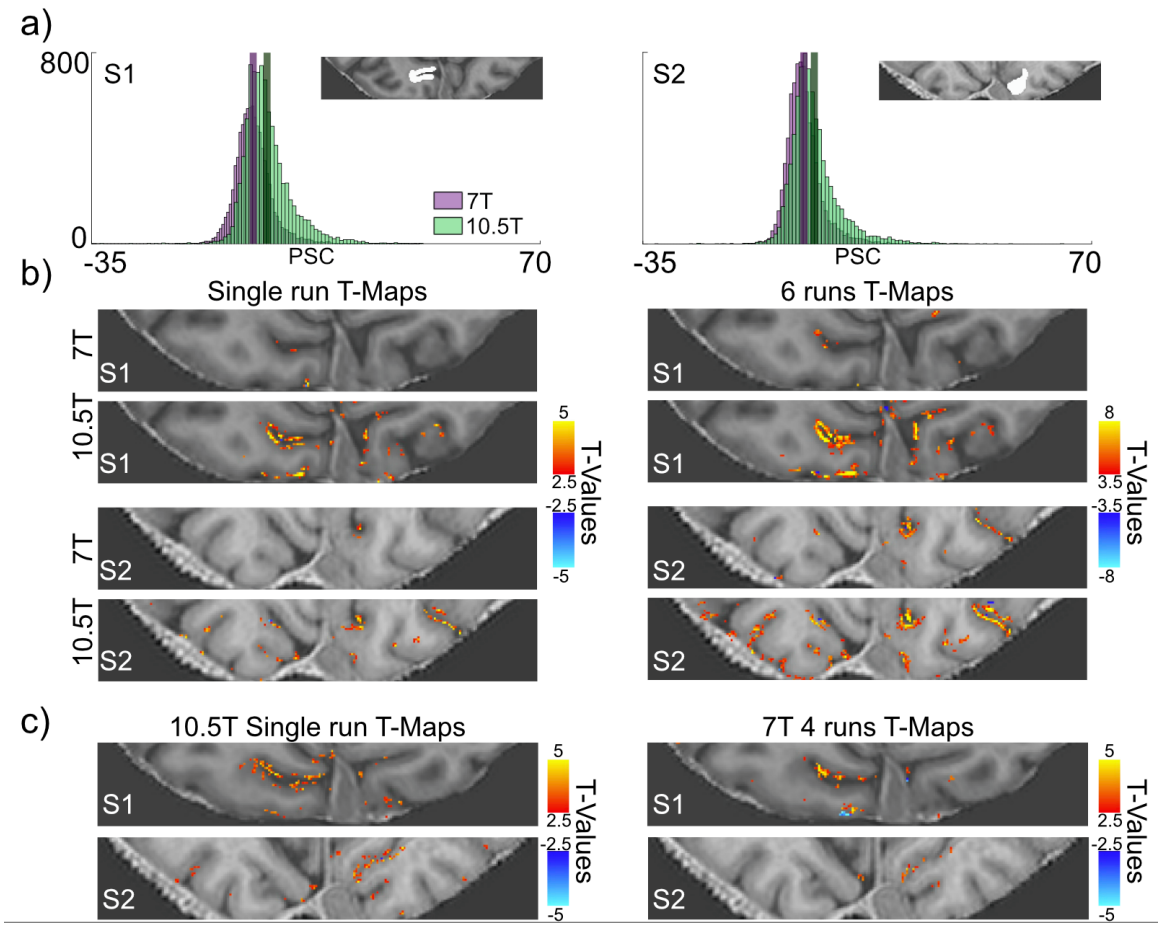

Figure 2: 0.4 mm isotropic functional imaging of retinotopically organized visual stimulation at 7T and 10.5T obtained with parameters iPAT=3; 5/8 pF; 40 Slices; TR=113ms; VAT=4972ms; TE=24.4ms for 7T and 10.5T, with minor variations in TR=111; VAT=4884; TE=24.2 for the latter. **(a)** Histograms of voxel-wise PSC (computed across 5 runs - i.e. 25 minutes of data) for the contrast Target and Surround >0 in 2 subjects. All voxels within the region of interest (example slice shown in the insert) were included. **(b)** 7T (top) and 10.5T (bottom) t-maps (cluster threshold of 5) superimposed on a co-registered MP2RAGE image for the contrast target and surround >0, for a single run (left panel) and for 6 concatenated runs (right panel). **(c)** Activation maps (t-maps elicited by target and surround > 0, cluster threshold of 5) superimposed on the co-registered MP2RAGE at 10.5T for a single run (~5 minutes of data) (left), and 4 runs (~20 mins of data) of 7T data (right) for 2 subjects. Note that different slices are displayed in panel b and c.

also report the t-maps for the same contrast for a single run (i.e. ~5 minutes) of 10.5T data and for 4 concatenated runs (~20 minutes) of 7T data (right panel).

2.3. 0.65 mm isotropic resolution GRE BOLD EPI images in auditory cortex at 10.5T

Figure 3 displays functional images during auditory stimulation at 0.65mm resolution, the highest resolution used for the auditory cortex to date (3D GRE-EPI) using a mixed fast-event related/block design auditory stimulation paradigm (see Methods). Although the EPI technique gets more challenging with increasing magnetic fields, high accelerations are possible with the synergistic use of high magnetic fields with high channel count arrays[19,54]; this in turn permits excellent quality EPI images even at 10.5T, as illustrated in Figure 3a and 3b.

A major challenge in high resolution GRE BOLD EPI acquisitions is keeping the echo time (TE) sufficiently short to achieve TE≈T2* so as to optimize the fCNR [5,52]. This requires the use of partial Fourier (pF) together with high accelerations along the phase encoding direction, as employed in the data presented in Figure 3 (5/8 partial fourier, iPAT=4). The standard approach uses zero-filling for the uncollected k-space data when pF is employed. This can potentially blur images, thus counteracting the effort to achieve high resolutions. Therefore, we developed an off-line reconstruction algorithm to handle this problem, which employed Projection Onto Convex sets (POCS)[55] to fill in the missing lines in pF, followed by NORDIC denoising[53] (see Methods). tSNR using POCS was lower, as expected, relative to standard vendor zero-padded images (Figure 3c top and middle panels, respectively). This SNR loss, however, was recovered using our tailored offline reconstruction, which includes POCS and NORDIC denoising (Figure 3c, bottom panel) (tSNR mean: 16.38 for Vendor (std: 5.99), 10.54 for POCS (std: 4.06), and 23.31 for offline (std: 11.41)).

Functional maps with a t-threshold (t>3.6) and a cluster threshold of 4 voxels for the sounds>0 contrast across the auditory cortex are shown in Figure 3d for 5 runs concatenated for

the tailored offline reconstructed images. Each run was approximately 8 min of data (i.e. 101 volumes). T-threshold was determined based on FDR correction (q<0.05).

We estimated the global smoothness within gray matter of EPI images in the fMRI time series using AFNI (3dFWHMx function)[56]. The spatial autocorrelation was estimated from the general linear model (GLM) residuals using a Gaussian+monoexponential decay mixed model to

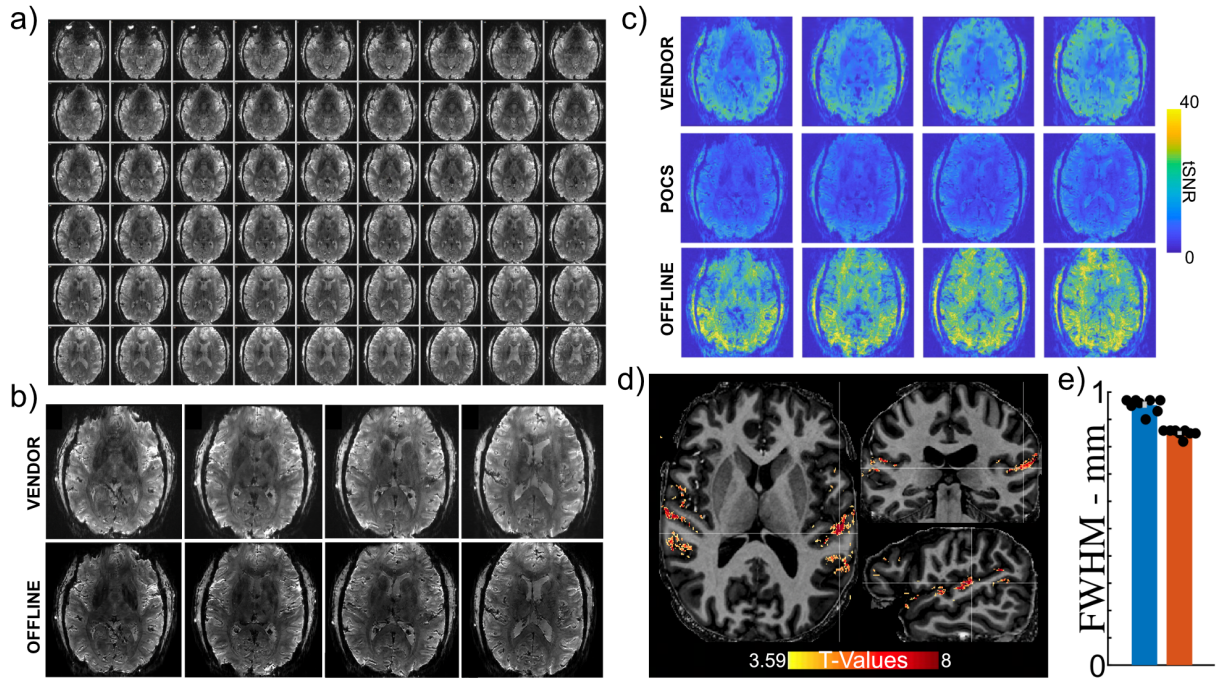

Figure 3: 0.65 mm isotropic (nominal) resolution GRE BOLD fMRI with auditory stimulation: TE=16.6 ms; TR=81 ms; in-plane acceleration iPAT=4; pF=5/8; 52 Slices; VAT (Volume Acquisition Time)=4536 ms, FOV=(272x276mm) **(a)** Vendor (online Dicoms) Single image EPI slices showcasing the achievable coverage (i.e. all slices). **(b)** Zoom in on selected single slices of a single EPI volume for vendor (online Dicoms) on the top and tailored offline reconstruction on the bottom row. **(c)** tSNR Maps for a single functional run after motion correction and linear detrending. **(d)** Activation to sounds (t-maps for sounds > 0) for 5 concatenated runs (just over 35 minutes of data) superimposed on a coregistered T1 (MP2RAGE) for the offline tailored reconstruction. **(e)** The average spatial blurring (i.e. autocorrelation in the GLM residuals) computed within the Grey Matter for 3 representative slices located towards the top, middle and bottom of the volume. The error bars show the standard error across 8 runs.

account for possible long-tail autocorrelations. The FWHM from this estimate, averaged over 8 runs after all data preprocessing steps (see Methods) was 0.95±0.026mm(std) for the Vendor and 0.86±0.014mm(std) for Offline, showing smoother images with zero-padding (paired t-test, $t(7) = 15.72$; $p < 0.001$). Hence, all subsequent data was processed with the Offline pipeline.

2.4. 0.35mm isotropic BOLD EPI images in visual cortex

Figure 4 displays 0.35mm (0.0428μL voxel) resolution (3D GRE-EPI) images for 2 participants, over the visual cortex for the same target-and-surround block design visual paradigm used in Figure 2. Figure 4a and top panel in Figure 4d show the t-maps for the target (in red) >surround (in blue) for subject 1 for 6 consecutive 5 min functional runs; functional maps are superimposed on slices from a single EPI volume in the fMRI time series. The lower panel in Figure 4d illustrates the same functional maps registered on an axial slice of the T_2* weighted images from the 0.37mm resolution ME-GRE acquisition. Single voxel time courses for a single 5min run for target-specific voxels are presented in Figure 4b, clearly displaying remarkably robust signal intensity changes selectively associated with the target stimulus epochs (dark blue bands). Figure 4c and 4d (bottom panel) show the t-maps (target > 0) evoked by single condition mapping for only 15 minutes of data for subject 2, superimposed on a selection of axial (top and middle panels in Figure 4c) and coronal (bottom panel Figure 4c) slices for the mean EPI, and on the ME-GRE (Figure 4d bottom). The green boxes in Figure 4c zoom into cortical regions demonstrating the separation of activation across adjacent banks of a sulcus (blue arrows), regardless of the presence (left most panel) or absence (middle panel) of large vessels, for single condition GRE BOLD-fMRI. Moreover, as previously reported[57], the green arrows in panel d indicate the Stria of Gennari, corresponding to layer 4 in V1, clearly visible as a dark stripe traversing the cortical ribbon for both subjects.

2.5. *Layer profiles and functional precision for 0.35mm and 0.8mm isotropic resolutions.*

Using the same visual stimuli employed in Figure 4, we also acquired 0.8mm resolution images at 7T in the same 2 subjects (see Methods). The global smoothness of the fMRI time series within the visual cortex in EPI images estimated using AFNI (3dFWHMx function)[56]. The functional resolution estimates (mean±Std) were 0.50±0.02mm (S1) and 0.42±0.01mm (S2) for the 10.5T 0.35mm data and 0.88±0.01mm (S1) and 0.90±0.02mm (S2) for the 7T 0.8mm data.

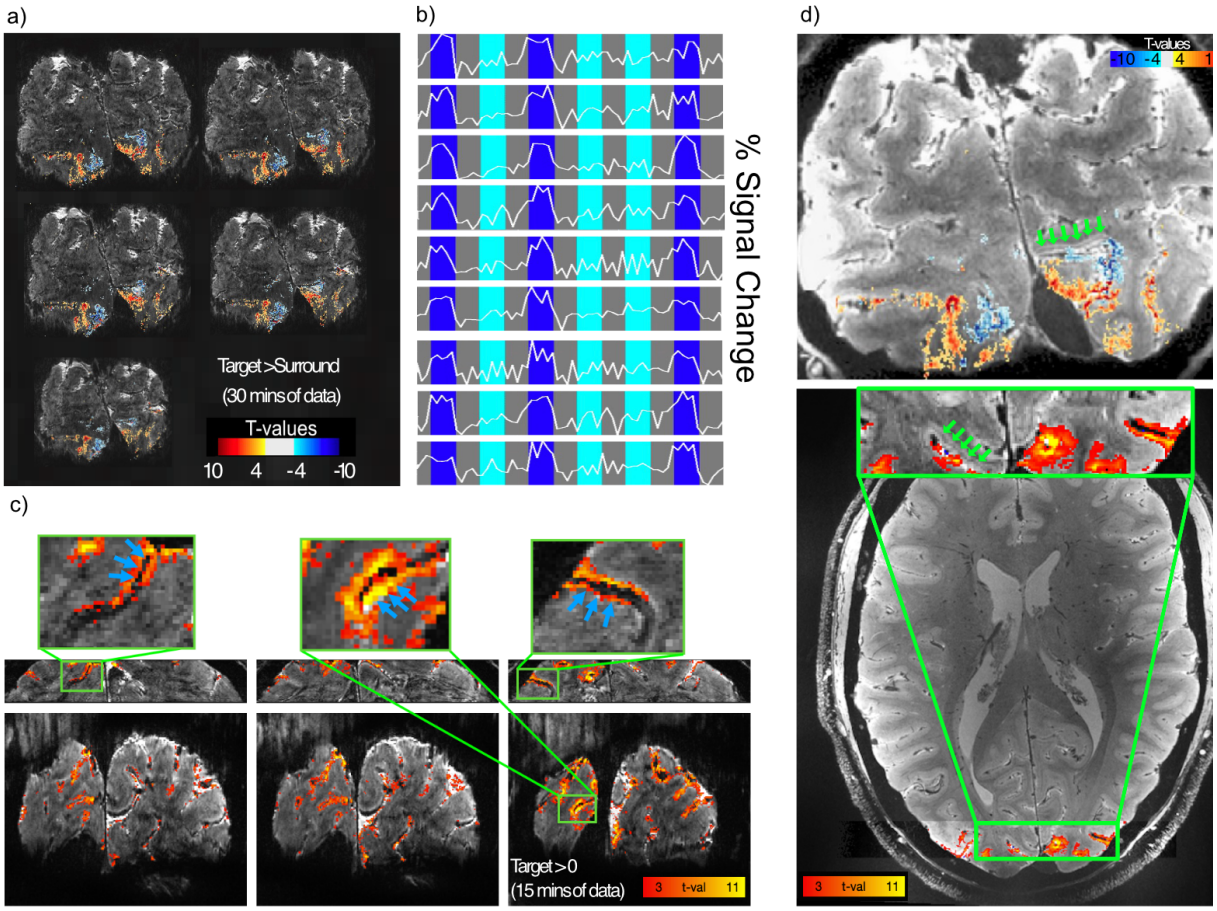

Figure 4. 0.35 mm resolution functional images at 10.5T acquired with iPAT=4; 5/8 PF; 40 Slices; TR=113ms; VAT=4972ms; TE=24ms. **(a)** Subject 1 (S1) t-maps for the contrast target>surround superimposed on single slices EPI images; **(b)** Examples of target-selective single-voxel single-run time courses; **(c)** S1 t-maps for the contrast target>0 superimposed on a selection of single slices mean EPI images; blue arrows on the zoom-in indicate how this resolution allows for the clear separation of the activation across adjacent banks of a sulcus, even for single condition maps, regardless of the presence (left and right most panel) or absence (middle panes) of large veins **(d)** top-panel: target>surround T-Maps for S1 superimposed on a T2* image; bottom panel: target>0 T-Maps for S2 superimposed on a T2* image; green arrows indicate the Stria of Gennari (dark line).

Two-sample t-tests carried out across runs independently per subject showed that the 10.5T 0.35mm data were significantly less smooth than the 0.8mm data (S1: $t(10) = -46.14$, $p<0.001$; S2: $t(10) = -49.87$, $p<0.001$).

We segmented the cortical ribbon into 13 depths within the retinotopic representation of the target stimulus in V1 with an equivolume approach (see Methods). The mean intensity of each depth for the 0.37mm ME-GRE images as well as for the mean EPI images of the fMRI times series across both resolutions are plotted in Figure 5a (top row). For both subjects, we observed a "*dip"* in the ME-GRE data at approximately 50% distance from the cerebrospinal fluid (CSF), corresponding to the afore mentioned Stria of Gennari. The same *"dip"* is clearly visible for the 0.35mm but not for the 0.8 mm resolution data in the EPI mean intensity values.

We further extracted the average PSC within depth elicited by each single block for all ~5min runs and present them individually (dotted red lines in Figure 5a). The average of these single-block PSC profiles is shown as a solid line. Note that the single blocks display essentially the same profile with little scatter. The laminar PSC data lead to three main observations:

First, the slopes of the ramping profile displaying increasing PSC towards the pial surface (i.e. towards CSF) – typical of GRE BOLD-fMRI - was significantly shallower for the 0.35 than the 0.8mm images (S1: (mean±Std) 0.35mm: 8.12±2.09, 0.8mm: 13.51±2.93, two-sample t-test: $t(22)=-5.20$, $p<0.001$; S2: (mean±Std) 0.35mm: 1.81±5.92, 0.8mm: 6.47±2.11, two-sample t-test: $t(22)=-2.57$, $p=0.0175$ – Figure 5). This was quantified by fitting a line to the PSC laminar profile elicited by each block and estimating its slope (see Methods). This result was primarily driven both by the apparent increase in evoked PSC amplitudes in the inner depths and the decreased amplitudes towards the pial surface for the 10.5T 0.35mm data, compared to the 0.8mm isotropic images.

Figure 5c illustrates the PSC in the 10.5T 0.35mm data for S2, over a larger depth distance, showing a rapid increase immediately beyond the GM-CSF boundary of the cortex.

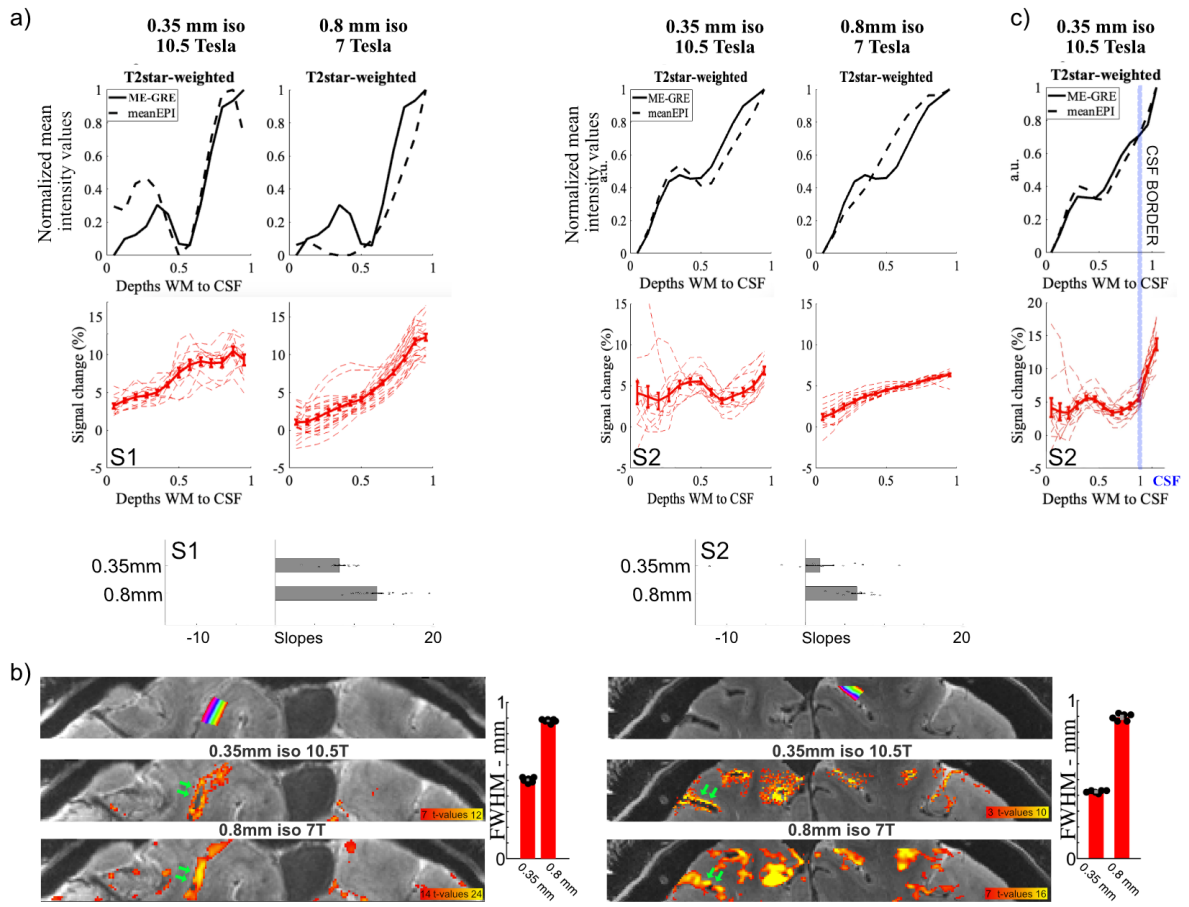

Figure 5. Comparison of 0.35 mm (10.5T) and 0.8 mm (7T) functional data. The upper row in panel **a** depicts laminar profiles of signal intensities for the T2*-weighted acquisitions (mean EPI and ME-GRE images) in two subjects. The dip in the middle depths seen in the 0.35 mm profiles identifies the location of the Stria of Gennari (layer IV), which is not visible in the corresponding 0.8 mm profile. The lower panel shows the functional PSC laminar profiles for the target condition. For both subjects, the 0.35 mm profiles demonstrate a bump co-localized with the layer IV dip in the T2*-weighted profiles. This bump was not resolved at 0.8 mm resolution. Furthermore, the unwanted vein-induced gradient towards superficial layers was significantly smaller at 0.35 mm than at 0.8 mm, as quantified in the adjacent bar plots showing the slopes of linear fits to the corresponding single-trial functional profiles; error bars represent standard error of the mean (SEM) across single trials. **b)** Illustration of the cortical layers used to extract laminar profiles in panel *a)* from an example slice in each subject (upper panel). The middle and lower panels show activation maps for the 0.35 and 0.8 mm acquisitions, respectively. The green arrows point to example locations where activation across adjacent sulcal banks is separable at 0.35 mm but not 0.8 mm resolution. Adjacent bar plots (panel b) depict the spatial autocorrelation-based blurring estimates, showing significantly lower smoothness in the 0.35 mm data; error bars represent SEM across imaging runs, which are shown as black dots. **c)** PSC in the 10.5T 0.35 mm data, showing a rapid increase immediately beyond the boundary between cortex and CSF (light-blue dotted line).

The 0.35mm and 0.8mm resolution functional maps for the two participants are shown in Figure 5b. As expected from a retinotopic paradigm such as the one employed here, the spatial extents and locations of activation look highly comparable across resolutions. However, the activation between adjacent banks of a sulcus (indicated by the green arrows in Figure 5b (also see Figure 4c)) is clearly separable for the 0.35mm 10.5T images but not for the 0.8mm 7T ones, which is blurred into a single cluster.

2.6. Whole-brain fMRI with 0.75mm resolution BOLD EPI

The data presented so far was obtained with 3D GRE EPI because of expected SNR advantages relative to slice-based acquisition. However, this approach leads to long volume acquisition times (VAT) for large FOVs. As such, the data presented in Figures 2 through 5 all used partial brain coverage, the extent of coverage decreasing with higher resolutions. For whole-brain coverage, slice-based Simultaneous Multi-Slice (SMS)/Multiband (MB) approach[58-60] can provide advantages for minimizing the volume acquisition time when high MB accelerations are feasible. As previously mentioned, 7T whole-brain studies typically use spatial resolution of >1 mm isotropic nominal resolutions. Here, we report whole-brain functional images obtained at 10.5T with a 0.75 mm isotropic resolution (i.e. 0.42μL), using SMS/MB GRE EPI acquisition with a temporal resolution (TR) of ~3.2 seconds (VAT is equal to TR in a 2D acquisition) (Figure 6). The acquisition parameters were: 0.75mm iso voxels; 12-fold 2D acceleration (MB=3; in-plane (iPAT)=4); 5/8 PF; 144 Slices; TR=3210ms; T=17.8). We used a 24-second on/off block design visual paradigm. Image acquisition and reconstruction was performed using the HCP Multiband reconstruction developed in CMRR (downloadable from https://www.cmrr.umn.edu/multiband/), *without denoising* and with minimal preprocessing (see Methods). Figure 6 shows the activation maps elicited by objects, bodies and faces within 37 minutes of data (i.e. 4 runs x ~9 min per run). Specifically, in panel 6a and 6b we report the voxels that were significantly active above baseline for the t-contrast faces $\cap$ bodies $\cap$ objects > 0 ($t(702)=3.10$; $q<0.05$ FDR corrected),

superimposed on a coregistered T1 weighted MP2RAGE[61] anatomical reference. Figure 6a shows statistically significant activation in the posterior cingulate cortex. The related time-course for a single run (~9 min) is shown as an insert in the middle panel of Figure 6a; the time course was averaged across all voxels under the crosshair. Figure 6b shows a statistically significant activation in different slices than those shown in Figure 6a; these slices were selected to illustrate activation in the prefrontal cortex and the related time-course for a single run, averaged across all voxels under the crosshair. By decreasing the t-threshold to $t(702)=2.5$ ($p=0.012$ uncorrected) we can detect activation bilaterally in the LGN (Figure 6c). The related single-run time-course reflects the average of all significantly active voxels for the left LGN only.

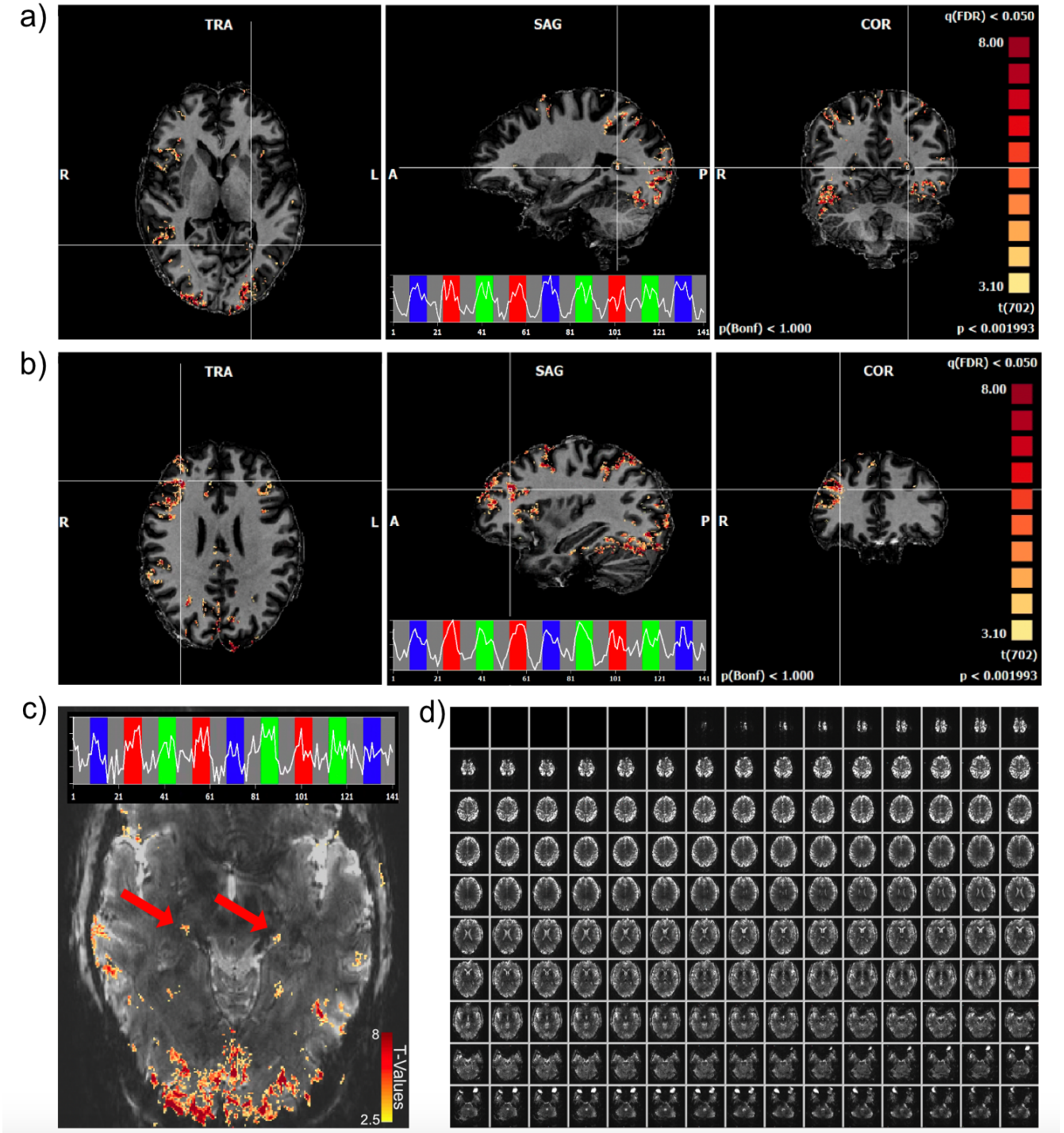

Figure 6: 0.75 mm isotropic whole-brain fMRI activation (t-maps) elicited by a visual task: objects, bodies and faces > 0, for approximately 37 minutes of data (without any denoising). **(a)** and **(b)** show activation maps in two different sets of three orthogonal slices (superimposed on coregistered MP2RAGE images) selected to show activation in the posterior cingulate cortex **(a)** and prefrontal cortex **(b).** The time-courses averaged for all voxels in the cluster identified by the crosshairs are shown for a single ~9 min run in the middle panel of both Figure 6a and 6b. **(c)** activation in bilateral LGN (red arrows) after 2-voxel smoothing superimposed on a single image EPI and related time-course in a single run. **(d)** Single slice EPI images for the whole volume.

3. DISCUSSION

Understanding the function of distributed large-scale brain networks that underly behavior ultimately requires information about the nature of the minimal architectural units that organize neural populations of similar properties. Such elementary cortical units exist in the mesoscopic scale, exemplified by complex but orderly organizations tangent to the cortical surface, such as the canonical orientation domains and the cortical columns that span the six layers of the ~1.5- to ~4-mm thick mammalian cortex. These meso-scale units are relevant also for untangling the mechanisms operative in pathological developments; for example, perturbations in layer-dependent computations that integrate feedforward, feedback and recursive circuital interactions have been proposed as models of dysfunction in neuropsychiatric disorders[62,63]. However, despite notable advances demonstrating feasibility, the ability to perform fMRI with sufficient resolution and fCNR to robustly access these meso-scale computations remains suboptimal, leading, as previously mentioned, to the incorporation of ambitious resolution targets in the strategic plan of the US BRAIN Initiative that are far beyond existing capabilities. Achieving such resolution goals requires significantly higher image SNR, substantial elevation in the intrinsically weak signal changes evoked by neuronal activity, and the ability to counteract the increasing acquisition-time demands of high-resolution imaging. It also requires remedies to imperfections inherent in the fMRI method that degrade the neuronal specificity of the functional signals. We demonstrate that the new frontier of beyond-10T magnetic fields, in this case 10.5 Tesla, addresses all these requirements and establishes a path forward for achieving major improvements in fMRI.

Ultimately, the ability to detect functional images is determined by fCNR ,which is given as $\Delta S/N$ where N is “noise” reflecting the fluctuations in the fMRI times series[14]. N is dominated by thermal noise at sufficiently high resolutions[64,65] (also see[53]); in this case, $\Delta S/N = (\Delta S/S)(SNR_{image})$ where SNR_{image} is the SNR of the images in the fMRI time series and $\Delta S/S$ is

fractional (or PSC) signal change coupled to neuronal activity. Both of these parameters increase at 10.5T.

In earlier work, we demonstrated that in going from 7T to 10.5T, theoretically maximal SNR (i.e. ultimate intrinsic SNR (uiSNR)) calculated in a human head model increases 1.4-fold peripherally, 2-fold at the edge of the brain, and 2.6-fold centrally[18]; the central gain was in agreement with the SNR measurements we made in the center of a sphere as a function of magnetic field strength[17]. We also demonstrated that these expected SNR gains can be captured with advanced, high channel count RF arrays[19,20], one of which was used in this study.

Functional images obtained with 0.4mm resolution (0.064μL volume) in 2 subjects illustrate that at the same TE, the 10.5T GRE BOLD response yields a ~2-fold higher PSC compared to 7T. Thus, enhanced image SNR and PSC together yield a ~4-to 5-fold multiplicative gain for fCNR in GRE BOLD-fMRI over the brain. In agreement, we observe significant improvements in t-values and the extent of activation detected for a given t-threshold (Figure 2) and the ability to probe robustly unprecedent resolutions, even without using NORDIC denoising (e.g. Figure 4 and 5 and Supplementary Figure S3). The supralinear gains in PSC also indicate the presence of significantly higher contributions from microvasculature to the BOLD effect; microvascular BOLD can have up to quadratic dependence on B_0 while the large vein contributions can only increase linearly with the magnetic field ([21], [22]).

As previously mentioned, the effective voxel dimensions typically exceed that of the nominal resolution. The reasons for such blurring include spatial smoothing along the phase encode dimension in EPI due to signal decay during the k-space acquisition. This mechanism is particularly concerning at high resolutions where the EPI echo train length (*etl*) gets longer, and at high magnetic fields where signal decay during the *etl* is faster due to the shorter T2* (Figure 1). As such, pushing to higher nominal resolutions with EPI-based fMRI can in fact lead to a decrease in effective resolution[66]. This problem can be countered using high-performance gradients[66] and/or a high degree of parallel imaging; in both cases, there is an SNR loss, which

is the same for the same reduction factor in *etl*. This loss comes from the higher bandwidth needed with high performance gradients for reducing *etl* and the fewer k-space data points collected with parallel imaging. The latter, however, has a limit due to the spatially non-uniform noise amplification by the g-factor[67]. However, ultrahigh fields (e.g.[20,68,69]) and high channel count arrays (e.g.[20,70,71]), as employed in this study, are particularly effective in suppressing the g-factor and promoting high accelerations. With this approach, we demonstrate that at 10.5T, even though there exists blurring, we are indeed gaining *effective* resolution when the *nominal* resolution is increased.

Depending on the region and the paradigm used, laminar profiles of functional signals should in principle display a peak in the middle layers (e.g.[72-74]) or two peaks associated with deeper and superficial layers[75]. Instead, progressively increasing PSC towards the pial surface is a renowned laminar feature of GRE BOLD fMRI (e.g.[72,73,75,76]), as demonstrated by the 0.8mm 7T data in Figure 5a. This is caused by the strong BOLD responses originating from the large draining-veins in the pial surface, which extend into the cortex and decrease with increasing distance from the pial surface. Nevertheless, due to its superior sensitivity, GRE BOLD remains the most popular acquisition protocol for fMRI, even for meso-scale studies, where the limited specificity is a real problem. Differential mapping can ameliorate, although not necessarily eliminate this problem, but requires suitable paradigms. Acquisition techniques such as spin-echo BOLD (e.g.[72,74,77-79]) and VASO [25,80] can suppress the large vessel contributions, but do so at the expense of large fCNR decreases. Here we show ultrahigh resolutions (0.35mm nominal) achieved at 10.5T for *single condition* GRE BOLD responses in fact suppress the draining-vein confound, as we predicted previously[53,81], yielding accurate cortical layer profiles. The evidence for this comes from several observations.

First, we observe a decrease in the slope of the layer profiles of the 0.35mm 10.5T fMRI data vs. the 7T 0.8mm images (Figure 5a). Second, we can clearly distinguish activation across adjacent banks of a sulcus for the 0.35mm 10.5T data but not for the 0.8mm 7T images (Figure

4c and Figure 5b). And finally, at 0.35mm, we are able to detect *features* across cortical layers that are not visible with standard 0.8mm resolution images. Specifically, we observe the presence of a mid-cortical maximum in PSC, appearing like a “bump” in the laminar profile of the 10.5T 0.35mm data, even in a ~5min run. This maximum, which is not visible in the 0.8mm 7T images, corresponds to the location of the Stria of Gennari and therefore to layer IV. As demonstrated by invasive animal studies, V1 receives direct feedforward inputs from the LGN at layer IV. As such, the larger activation in layer IV is precisely what is expected from pure visual feedforward stimulation as implemented here.

There are two reasons for this improved specificity and layer profiles. One is a magnetic field effect, namely the supralinearly increasing microvascular contribution at the higher magnetic fields. The second is a resolution effect, the existence of which was discussed in our previous publications[53,81] and is more extensively presented here in the Supplementary Material Section. The extravascular BOLD (EV-BOLD) phenomenon dominates BOLD based fMRI maps at ultrahigh magnetic fields (e.g.[22 82]); it generates fMRI signals through the intra-voxel dephasing of spins due to magnetic field inhomogeneities induced outside deoxyhemoglobin containing blood vessels. In the limit voxel dimensions become small compared to the distances that characterize these magnetic field gradients associated with EV-BOLD, magnetic fields *inside* the voxels become more uniform, suppressing the BOLD response. This is particularly true with increasing distance from the blood vessel as the magnetic field gradient becomes shallower. A prediction of this effect is that the BOLD effect associated with pial veins shrinks in spatial extent, persisting only in close proximity to the blood vessel boundaries where the magnetic field gradient is steepest (see Supplementary Material Section). Thus, as resolutions increase, draining-vein effects get concentrated in the pial surface, and penetrate less into the cortex. This is indeed what is observed in the 0.35mm data where the PSC rapidly rises just beyond the outer cortical boundary in the space where the pial veins reside (Figure 5c).

This resolution effect can also be conceptualized using simple GRE images of a brain slice where signal intensity dropouts occur near the air-filled cavities at low but not high resolutions as discussed in Supplementary Figure S2.

It would be ideal to use such high-resolution data for defining brain-wide networks with layer specificity, using Human-Connectome-Project (HCP) style whole-brain acquisitions. However, even with the high accelerations available from 10.5T and high channel count arrays, nominal resolutions such as 0.35mm lead to undesirably long volume acquisition times. Nevertheless, compromises are possible that provide significant improvement over the 1.6mm resolution 7T HCP resting-state and task-based fMRI acqusitions[59,83]. Here, we demonstrate the feasibility of next generation HCP style high-resolution, whole-brain fMRI, one that can achieve sub-millimeter (0.75mm) resolutions with TRs of 3s, while also maintaining sufficient functional sensitivity. We used 2D multi-slice GRE SMS/MB EPI, exploiting combined through-plane (i.e. multiband, MB[58]) and in-plane acceleration (12 fold 2D acceleration), to decrease TE and TR, thus reducing the image acquisition times to practical levels. Single subject functional images obtained in ~30 min with this protocol display robustly detectable activity evoked by objects, bodies and faces, extensively through the brain, ranging from LGN, visual cortex, temporal lobes, parietal lobes, prefrontal cortex etc. (Figure 6). Functional mapping at these spatial and temporal resolutions and coverage in single subjects represents an unprecedented opportunity for human neuroscience.

4. CONCLUSION

In conclusion, we present initial results from 10.5T GRE BOLD-fMRI demonstrating major increases in fCNR, achievable resolution, and spatial precision of functional mapping, exploiting the major gains in intrinsic SNR and image acceleration available for brain studies at 10.5T. We also demonstrate that high spatial resolutions suppress the draining-vein confound of the GRE BOLD-fMRI improving its specificity relative to neuronal activity. The results presented usher in

the gains that are available in the new era of beyond 10 Tesla human functional imaging, particularly for mesoscale fMRI studies. Further improvements in effective resolutions and temporal sampling (i.e. acceleration) are possible when such extremely high fields will be combined with the use of higher performance gradients, and further developments in image reconstruction and denoising strategies, such as those based on deep learning(e.g.[84,85]).

5. METHODS

5.1. Experimental paradigms

5.1.1. Block design retinotopically organized visual stimulation with flickering gratings

The experimental procedure consisted of a 24-seconds on/off block design for the 0.4 mm isotropic 7T/10.5T acquisitions and for the 10.5T 0.35 mm isotropic voxel acquisitions. For the 7T 0.8 mm isotropic resolution dataset the durations were 12s on and 12s off for S1. The difference in block length was implemented to account for the difference in volume acquisition time between the 0.8 mm and the other acquisitions (see later). For S2 we acquired the 7T 0.8 mm images with identical timings as the 10.5T 0.35 mm images (i.e. 24 seconds on/off). The stimuli consisted of a center (i.e. target) and a surround square checkerboard counterphase flickering (at 6 Hz) gratings subtending approximately 5.6 degrees of visual angle. Stimuli were centered on a background of average luminance (25.4 cd/m^2, 23.5-30.1). Using a Mac Pro computer, stimuli were presented on a Cambridge Research Systems BOLDscreen 32 LCD monitor positioned at the head at 7T (resolution 1920, 1080 at 120 Hz; viewing distance ~89.5 cm.) and using a VPIXX projector at 10.5T (resolution 1920, 1080 at 60 Hz; viewing distance ~89.5 cm.). Stimulus presentation was controlled using Psychophysics Toolbox (3.0.15) codes. Participants viewed the images through a mirror placed in the head coil.

Each run began and ended with a red fixation dot centered on a gray background and consisted of 3 trials for each of the 2 conditions. This resulted in eight ~2.5-minute runs for the 12 seconds on/off acquisition (i.e. S1's 0.8 mm 7T data) and just over 5-minute runs for the 24 seconds on/off acquisitions (6 runs). Participants were instructed to minimize movement and keep fixation locked on the center fixation dot throughout the experimental runs.

5.1.2. Block design visual stimulation with objects, bodies and faces

The experimental procedure implemented for the whole-brain isotropic 0.75 mm acquisition consisted of a standard 24-second on/off block design. The stimuli consisted of a set of face images, bodies without faces, and objects, subtending approximately 5° of visual angle. We equated the amplitude spectrum across all images. The stimuli were centered on a background of average luminance (25.4 cd/m^2, 23.5-30.1) and were presented using a Mac Pro computer and a VPIXX projector (see above). Stimulus presentation was controlled using Psychophysics Toolbox (3.0.15). Participants viewed the images through a mirror placed in the head coil.

Each run began and ended with black fixation cross centered on a gray background and consisted of 3 trials for each of the 6 conditions (~9 minutes duration). We collected 4 experimental runs. Participants were instructed to minimize movement and keep fixation locked on the center fixation dot throughout the experimental runs. This experimental paradigm was adapted from [86].

5.1.3. Auditory stimulation

We adapted (using cascading sequences) the classical local-global paradigm that has been used previously to study the effects of local and global expectations on 'error-related' responses [87]. Each trial consisted of a sequence of 4 sounds (100 ms per sound with a 100 ms gap in between) that was presented over a total of 700 ms, followed by a 500 ms gap before the next trial started. For each sequence, the first three sounds were presented in an ascending or descending order in acoustic frequency with the fourth tone either following this ascending or descending pattern (locally standard trials) or violating this pattern (locally deviant trials). In distinct experimental blocks of 3 minutes each, global regularity was defined according to the presentation rate of each stimulus. Globally standard trials were presented 90% of the time, whereas globally rare stimuli were pseudo randomly presented 10% of the time. Four types of trials were created by manipulating local and global regularities: local and global standard, local and global deviant, local standard but global deviant, and local deviant but global standard.

To account for the presentation rate of each frequency, in each block we presented two types of globally standard trials (e.g. frequencies [1 2 3 4] and [2 3 4 5]) that were presented pseudo-randomly. In between globally deviant trials (e.g. frequencies [2 3 4 1]), we always presented either 8, 9 or 10 globally standard trials. Each block started with 30 habituation trials (not counted towards the 90%-10% regularity rule) to establish the global regularity before presenting the first globally deviant trial. Each run consisted of two blocks, one in which the globally standard trials were also locally standard (e.g. [1 2 3 4] and [2 3 4 5]) and alternatively one block in which globally standard trials were locally deviant (e.g. [2 3 4 1] and [3 4 5 2]) and the globally deviant trials were locally standard (e.g. [2 3 4 5]). The order of blocks, and the ascending and descending cascades were counterbalanced. Each run lasted approximately 8 minutes and we recorded a total of 8 experimental runs.

5.2 MR Imaging Acquisition and Processing

The 0.8 mm^3 7T functional MRI data were collected with a 7T Siemens Magnetom System with a single transmit and 32-channel receive NOVA head coil, while the 0.4 mm^3 were collected with a 7T Terra System with a single channel in-house built 64-channel receive head coil [18,19,88]. All 10.5T MRI data were collected with a 10.5T Siemens Magnetom System with an in-house built 16 transmit and 80 receive -channel head coil [18,19,88]. The in-house developed 10.5T and 7T array coils have been extensively characterized in terms of performance [18,19,88].

5.2.1. 10.5T acquisition protocols

Below we list the acquisition parameters for all protocols:

0.65mm isotropic nominal resolution fMRI: 3D GRE EPI; TE=16.6ms; TR=81ms; in-plane acceleration factor along the phase encode direction (iPAT) =4; pF=5/8; 52 Slices; VAT (Volume Acquisition Time)=4536ms; FA=14deg

0.4 mm isotropic nominal resolution fMRI: 3D GRE EPI; iPAT=3; 5/8 PF; 40 Slices; TR=111ms; VAT=4884s; TE=24.2ms; FA=15deg

0.35 mm isotropic nominal resolution fMRI: 3D GRE EPI; iPAT=4; 5/8 PF; 40 Slices; TR=113ms; VAT=4972 ms; TE=24ms; FA=15deg

0.75mm isotropic nominal resolution fMRI: 2D SMS/MB GRE EPI; iPAT=4; MB3; 5/8 PF; 144 Slices; TR=3210ms; TE=17.8ms; FA=75deg

MP2RAGE Anatomical imaging: 0.7mm isotropic voxels; TR=5000ms; TE=1970ms; Acquisition time: 07:30; FoV=253*270mm; iPAT=4; Inversion 1=840ms; Inversion 2=2370ms; Partial Fourier 6/8; FA 1=6deg; FA 2=6deg

Multi Echo (ME) GRE acquisition with 0.37 mm isotropic resolution: to estimate T2* values, whole brain data on two subjects were obtained with a 3D ME-GRE acquisition with 7 echoes: TEs: 4.07, 7.95, 11.83, 15.71, 19.59, 23.47, 27.35ms; TR=33ms. In the following acquisitions geared towards identifying the Stria of Gennari rather than estimate T2* values, we only acquired 6 echoes (TEs; 4.1, 7.9, 12, 16, 20, 23ms; TR=29ms). This shortened the acquisition time, without impacting SNR and the localization of the Stria. The remaining acquisition parameters were kept constant: FA=10deg; 7/8ths partial Fourier; 2D acceleration (in-plane and through-plane) GRAPPA: 3x3; Matrix $(k_x \times k_y \times k_z)$=576x576x320, with k_z designating the through-plane "slice" direction.

ME GRE acquisitions 0.8 mm isotropic resolution: Whole-brain data on three subjects were obtained with 3D ME-GRE using parameters: TEs: 4, 8, 12, 16, 20, 24, 28ms; TR=33ms; FA=10deg; 7/8ths partial Fourier; GRAPPA: 3x2; Matrix$(k_x \times k_y \times k_z)$=264x264x240 with k_z designating the through-plane "slice" direction.

5.2.2. 7T acquisition protocols

0.4mm isotropic nominal resolution fMRI: 3D GRE EPI; iPAT=3; 5/8 PF; 40 Slices; TR=113ms; VAT=4972ms; TE=24.4ms; FA=16deg

0.8mm isotropic nominal resolution fMRI: 2D GE EPI; 42 slices; TR=1350 ms; Multiband factor 2, iPAT 3; 6/8ths Partial Fourier; TE=26.4ms; FA=70deg

ME GRE acquisitions 0.35 mm isotropic resolution: Six acquisitions, partial field of view (axial slab, roughly aligned to AC-PC line) multi-echo 3D GRE images were obtained using a 32 Channel NOVA head coil. TEs 4.37, 8.74, 13.11, 17.48, 21.85, 26.22ms; TR=32ms; FA=12deg; no partial Fourier; GRAPPA 2x2. Matrix($k_x \times k_y \times k_z$)= 576 x 576 x 160 with k_z designating the through-plane "slice" direction.

5.3 ME GRE data processing for calculation of T2* values

Processing: Due to the bipolar readout, visible distortion was present in odd versus even echoes at 10.5T. To correct for this, we calculated nonlinear alignments between the odd and even echoes (correcting to the intermediate space) using the SyN approach in the antsRegistration package. To align across runs, both rigid and nonlinear alignment was calculated, using the same package. A final alignment step to the anatomical space from which regions of interest were defined (described below) was also calculated using the same tool. All transforms were combined and applied in a single step to prevent blurring from multiple interpolation steps. These steps follow current best practices for the analysis of such high-resolution data[57].

Following the transformation, a grand mean was calculated for each echo across the 2 or 3 separate runs.

For the 7T data, distortions were minimal in our regions of interest, and therefore nonlinear methods were not used. Instead, the mean of each run was rigidly aligned to the first run and then to the anatomical space. Following the transformations, a grand mean was calculated for each

echo across the 6 separate runs. Finally, both the 7T and 10.5T data were aligned into the same space for comparison.

T2 Fits:* T2* fits were estimated using the function t2smap from the python package tedana, using the nonlinear curve fitting approach, which is slower but expected to be more accurate than the typical log-linear approximation. These T2* estimates were then used to produce a weighted average of the input data.

Regions of Interest: A mask of the gray matter (GM) ribbon was produced at high resolution (0.37mm) using the surfaces (smoothwm, pial) derived from FreeSurfer. Labels for white matter (WM) and insula areas were derived from the automatic labeling performed by Freesurfer, after upsampling to the 0.37mm space. The label from V1 was produced using the Benson Atlas automated label approach. For GM/WM comparisons a final inclusion mask was manually drawn to include only areas with sufficient signal in the 0.37mm 10.5T data. To produce cortical depths, the high-resolution GM ribbon, along with WM and CSF labels was passed through LN2_LAYERS - a part of the LayNii toolbox, using equivolume depth calculations. The metric file, which contains a cortical depth estimate for each voxel within the GM, was then used to extract depth-dependent metrics from the weighted average and T2* estimates.

5.4 Functional data Preprocessing

All functional data preprocessing was performed using BrainVoyager, AFNI and ANTs. Preprocessing was kept at a minimum and consistent across reconstructions. Specifically, we performed slice scan timing corrections for the 2D data only (temporal sinc interpolation), 3D rigid body motion correction (spatial sinc interpolation) where all volumes for all runs were motion corrected relative to the first volume of the reference run, and low drift removal (i.e. temporal high pass filtering) was performed using a GLM approach with a design matrix continuing up to the 3rd order discrete cosine transform basis set. No spatial nor temporal smoothing was applied.

Functional and anatomical data (MP2RAGE and ME-GRE) were aligned using AFNI and ANTs with manual adjustments and iterative optimizations.

Temporal SNR was computed by dividing the mean (over time) of the detrended time-courses by its standard deviation independently per voxel, run and subject.

To quantify the extent of stimulus-evoked activation, we performed standard GLM estimation (with ordinary least squares minimization) using BrainVoyager or AFNI. Paradigm regressors of the design matrices were generated by convolution of a double gamma function with a "boxcar" function (representing onset and offset of the stimuli). Subsequent analyses (i.e. ROI-based and statistical testing) were performed in MatLab using a set of tools developed in-house.

5.5 ROI definition and cortical depth segmentation

0.4mm isotropic voxel images: We further performed region of interest (ROI) analyses to compare evoked percent signal changes (PSC) across all voxels within the ROI. To avoid biasing the ROI definition to either field strength, we defined our cortical region anatomically, guided by functional contrast maps. Specifically, the ROI was derived as follows: After co-registering both the 10.5T and the 7T functional data to the same MP2RAGE image, to identify the retinotopic representation of both stimuli in V1 we performed the contrast target & surround > 0 of run1 independently for each field strength (which was excluded from subsequent analyses). We used both t- as well as PSC maps at different thresholds across field strengths as to maximize overlap between evoked activation. Guided by the contrast maps, we then relied on Benson probabilistic atlas to identify V1 and proceeded to draw an anatomically informed ROI based on V1 delineations on the coregistered T1 image.

GLM t-values can be approximately conceptualized as beta estimates divided by GLM standard error according to this equation:

$$t = c'b/\sqrt{\mathrm{Var}(e)c'(X'X)^{-1}c} \quad \text{(eq. 1)}$$

where b represents the beta weights, c is a vector of 1, -1 and 0 indicating the conditions to be contrasted, e is the GLM residuals and X the design matrix.

Two-sample two-sided t-tests (across single-trial PSC estimates) were used to test for within-subject differences in PSC between the two field strengths.

0.8mm and 0.35mm isotropic voxel images: The ROI used for laminar analyses was defined in a portion of V1 corresponding to the retinotopic representation of the target condition. V1 was identified based on a clear manifestation of the Stria of Gennari in the 0.35 mm resolution mean EPI and ME-GRE images. The target representation was selected as a patch of cortex demonstrating robust target-preference based on the target>surround contrast maps. Note that the first two runs were used for ROI definition and thus discarded in subsequent laminar analyses. Voxel-wise cortical depth estimates were obtained using LAYNII's LN2_LAYERS [89], based on manually-drawn WM and CSF boundaries. These were drawn around the ROI on an upsampled 0.2 mm isotropic grid. Laminar profiles were then computed by averaging the single-trial PSC estimates (target > fixation) of ROI voxels within each of 13 equivolume depth bins. For S1, the number of trials used in activation maps and laminar profiles was 12 and 24 for the 0.35 mm and 0.8 mm datasets, respectively, to thereby match the total functional scan time.

Gradient echo BOLD is plagued by contamination of unwanted venous BOLD, resulting in increased PSC in proximity of the pial surface (where large draining vessels are concentrated), giving rise to the renown GE BOLD laminar ramping profile. To estimate the impact of draining vessels across resolutions, we quantified the slope of the amplitude ramping profiles across depths as follows: we performed a linear fit to the laminar profiles for each trial and resolution and estimated the slopes of the fitted lines using MATLAB's *regress*-function. Two-sample two-sided t-tests (across single-trial slope estimates) were used to evaluate for within-subject differences in

slopes between the two resolutions. Note that for S1 only the first 12 trials in the 0.8 mm dataset were used in this t-test to match sample size across resolutions.

5.6 Quantifying BOLD images smoothness

Global smoothness measures were obtained to compare the estimated differences in functional blurring between different reconstructions (Vendor versus Offline in the 0.65mm datasets) and between different resolutions (0.35mm versus 0.8mm). Smoothness estimates were obtained from the GLM residuals, using the function 3dFWHMx from AFNI[90] with the '-ACF' command. This method estimates the spatial autocorrelation from the data using a Gaussian plus mono-exponential model, which accounts for possible long-tail spatial autocorrelations. The estimated FWHM, in mm, from this fitted autocorrelation function is used as an estimate of the smoothness of the data. This estimate was derived from individual runs. Across-run paired sample two-sided t-tests for the reconstruction comparison, and across-run two-sample two-sided t-tests for the resolution comparison were carried out between estimated FWHM parameters to infer statistical significance.

5.7 Tailored off-line reconstructions

The 3D-EPI was obtained with monotonic sampling of the slice-phase encoding direction and preceding each EPI readout a 3-line navigator was acquired without any phase-encoding. Each temporal multi-channel data sample was decorrelated based on the correlation estimate from a noise-only acquisition. Each EPI readout train was corrected for timing precision using a linear phase obtained from the 3-line navigator, with the same correction applied for all channels. Phase-encoding undersampling was corrected using a two-step GRAPPA implementation, where firstly the missing lines were calculated, and then the acquired data were re-estimated from the neighboring measurements, analogous to a 1-step SPIRIT. Ramp-sampling correction of each readout line was applied using a spline interpolation to the Nyquist sampling. A 1D FFT was

applied in the slice-encoding direction. POCS partial Fourier reconstruction [55] was applied for each channel and each slice, and the reconstructed images were combined using a SENSE-1 algorithm with ESPIRIT estimated sensitivity profiles. NORDIC denoising was applied to the complex valued time-series as described in [91], where the g-factor and noise were estimated using an implementation of the MPPCA algorithm.

5.8 Participants

We acquired 8 functional and 7 structural data sets on 4 healthy right-handed subjects (age range: 28-50), with different stimulation paradigms, acquisition parameters and field strengths (see *above*). All subjects had normal or corrected vision and provided written informed consent. The study complied with all relevant ethical regulations for work with human participants. The local IRB at the University of Minnesota approved the experiments.

ACKNOWLEDGEMENTS: This work was supported by NIH grants R01 NS136490 (L.V.), U01 EB025144. (K.U.), U01NS137991 (E.Y.), P41EB027061 (K.U.), S10RR029672 (K.U) and UM1 NS132207-01 (K.U. and E.Y.)

COMPETING INTEREST: The authors confirm that there are no competing interests.

DATA AVAILIBILITY: The data that support the findings of this study are available from the corresponding author upon reasonable request, subject to human subjects IRB limitations.

CODE AVAILIBILITY: The image reconstructions codes that support the findings of this study are available here: https://www.cmrr.umn.edu/downloads/.

6. REFERENCES

1 Ogawa, S. *et al.* Intrinsic signal changes accompanying sensory stimulation: functional brain mapping with magnetic resonance imaging. *Proc Natl Acad Sci U S A* **89**, 5951-5955, doi:10.1073/pnas.89.13.5951 (1992).

2 Kwong, K. K. *et al.* Dynamic magnetic resonance imaging of human brain activity during primary sensory stimulation. *Proc Natl Acad Sci U S A* **89**, 5675-5679, doi:10.1073/pnas.89.12.5675 (1992).

3 Gordon, E. M. *et al.* Precision Functional Mapping of Individual Human Brains. *Neuron* **95**, 791-807 e797, doi:10.1016/j.neuron.2017.07.011 (2017).

4 Naselaris, T., Allen, E. & Kay, K. Extensive sampling for complete models of individual brains. *Current Opinion in Behavioral Sciences* **40**, 45-51, doi:10.1016/j.cobeha.2020.12.008 (2021).

5 Menon, R. S., Ogawa, S., Tank, D. W. & Ugurbil, K. Tesla gradient recalled echo characteristics of photic stimulation-induced signal changes in the human primary visual cortex. *Magn Reson Med* **30**, 380-386, doi:10.1002/mrm.1910300317 (1993).

6 Turner, R. How much cortex can a vein drain? Downstream dilution of activation-related cerebral blood oxygenation changes. *Neuroimage* **16**, 1062-1067 (2002).

7 Bianciardi, M., Fukunaga, M., van Gelderen, P., de Zwart, J. A. & Duyn, J. H. Negative BOLD-fMRI signals in large cerebral veins. *J Cereb Blood Flow Metab* **31**, 401-412, doi:10.1038/jcbfm.2010.164 (2011).

8 Ugurbil, K. What is feasible with imaging human brain function and connectivity using functional magnetic resonance imaging. *Philos Trans R Soc Lond B Biol Sci* **371**, doi:10.1098/rstb.2015.0361 (2016).

9 Kay, K. *et al.* A critical assessment of data quality and venous effects in sub-millimeter fMRI. *Neuroimage* **189**, 847-869, doi:10.1016/j.neuroimage.2019.02.006 (2019).

10 Olman, C. A., Inati, S. & Heeger, D. J. The effect of large veins on spatial localization with GE BOLD at 3 T: Displacement, not blurring. *Neuroimage* **34**, 1126-1135, doi:10.1016/j.neuroimage.2006.08.045 (2007).

11 Shmuel, A., Yacoub, E., Chaimow, D., Logothetis, N. K. & Ugurbil, K. Spatio-temporal point-spread function of fMRI signal in human gray matter at 7 Tesla. *Neuroimage* **35**, 539-552, doi:10.1016/j.neuroimage.2006.12.030 (2007).

12 Kay, K., Jamison, K. W., Zhang, R. Y. & Ugurbil, K. A temporal decomposition method for identifying venous effects in task-based fMRI. *Nat Methods* **17**, 1033-1039, doi:10.1038/s41592-020-0941-6 (2020).

13 Ugurbil, K. Magnetic resonance imaging at ultrahigh fields. *IEEE Trans Biomed Eng* **61**, 1364-1379, doi:10.1109/TBME.2014.2313619 (2014).

14 Ugurbil, K. Imaging at ultrahigh magnetic fields: History, challenges, and solutions. *Neuroimage* **168**, 7-32, doi:10.1016/j.neuroimage.2017.07.007 (2018).

15 Vaughan, J. T. *et al.* 7T vs. 4T: RF power, homogeneity, and signal-to-noise comparison in head images. *Magn Reson Med* **46**, 24-30 (2001).

16 Pohmann, R., Speck, O. & Scheffler, K. Signal-to-noise ratio and MR tissue parameters in human brain imaging at 3, 7, and 9.4 tesla using current receive coil arrays. *Magn Reson Med* **75**, 801-809, doi:10.1002/mrm.25677 (2016).

17 Le Ster, C. *et al.* Magnetic field strength dependent SNR gain at the center of a spherical phantom and up to 11.7T. *Magn Reson Med* **88**, 2131-2138, doi:10.1002/mrm.29391 (2022).

18 Zhang, B. *et al.* Performance of receive head arrays versus ultimate intrinsic SNR at 7 T and 10.5 T. *Magn Reson Med* **92**, 1219-1231, doi:10.1002/mrm.30108 (2024).

19 Waks, M. *et al.* RF coil design strategies for improving SNR at the ultrahigh magnetic field of 10.5T. *Magn Reson Med* **93**, 873-888, doi:10.1002/mrm.30315 (2025).

20 Lagore, R. L. *et al.* A 128-channel receive array with enhanced signal-to-noise ratio performance for 10.5T brain imaging. *Magn Reson Med* **93**, 2680-2698, doi:10.1002/mrm.30476 (2025).

21 Ogawa, S. *et al.* Functional brain mapping by blood oxygenation level-dependent contrast magnetic resonance imaging. A comparison of signal characteristics with a biophysical model. *Biophys J* **64**, 803-812, doi:10.1016/S0006-3495(93)81441-3 (1993).

22 Uludag, K., Muller-Bierl, B. & Ugurbil, K. An integrative model for neuronal activity-induced signal changes for gradient and spin echo functional imaging. *Neuroimage* **48**, 150-165, doi:10.1016/j.neuroimage.2009.05.051 (2009).

23 Dumoulin, S. O., Fracasso, A., van der Zwaag, W., Siero, J. C. W. & Petridou, N. Ultra-high field MRI: Advancing systems neuroscience towards mesoscopic human brain function. *Neuroimage* **168**, 345-357, doi:10.1016/j.neuroimage.2017.01.028 (2018).

24 De Martino, F. *et al.* The impact of ultra-high field MRI on cognitive and computational neuroimaging. *Neuroimage* **168**, 366-382, doi:10.1016/j.neuroimage.2017.03.060 (2018).

25 Huber, L. *et al.* Layer-dependent functional connectivity methods. *Prog Neurobiol* **207**, 101835, doi:10.1016/j.pneurobio.2020.101835 (2021).

26 Zaretskaya, N. Zooming-in on higher-level vision: High-resolution fMRI for understanding visual perception and awareness. *Prog Neurobiol* **207**, 101998, doi:10.1016/j.pneurobio.2021.101998 (2021).

27 Lawrence, S. J. D., Formisano, E., Muckli, L. & de Lange, F. P. Laminar fMRI: Applications for cognitive neuroscience. *Neuroimage* **197**, 785-791, doi:10.1016/j.neuroimage.2017.07.004 (2019).

28 Norris, D. G. & Polimeni, J. R. Laminar (f)MRI: A short history and future prospects. *Neuroimage* **197**, 643-649, doi:10.1016/j.neuroimage.2019.04.082 (2019).

29 Polimeni, J. R. & Uludag, K. Neuroimaging with ultra-high field MRI: Present and future. *Neuroimage* **168**, 1-6, doi:10.1016/j.neuroimage.2018.01.072 (2018).

30 Weldon, K. B. & Olman, C. A. Forging a path to mesoscopic imaging success with ultra-high field functional magnetic resonance imaging. *Philos Trans R Soc Lond B Biol Sci* **376**, 20200040, doi:10.1098/rstb.2020.0040 (2021).

31 Finn, E. S., Huber, L. & Bandettini, P. A. Higher and deeper: Bringing layer fMRI to association cortex. *Prog Neurobiol* **207**, 101930, doi:10.1016/j.pneurobio.2020.101930 (2021).

32 Self, M. W., van Kerkoerle, T., Goebel, R. & Roelfsema, P. R. Benchmarking laminar fMRI: Neuronal spiking and synaptic activity during top-down and bottom-up processing in the different layers of cortex. *Neuroimage* **197**, 806-817, doi:10.1016/j.neuroimage.2017.06.045 (2019).

33 Poplawsky, A. J., Fukuda, M. & Kim, S. G. Foundations of layer-specific fMRI and investigations of neurophysiological activity in the laminarized neocortex and olfactory bulb of animal models. *Neuroimage* **199**, 718-729, doi:10.1016/j.neuroimage.2017.05.023 (2019).

34 Yacoub, E., Harel, N. & Ugurbil, K. High-field fMRI unveils orientation columns in humans. *Proc Natl Acad Sci U S A* **105**, 10607-10612, doi:10.1073/pnas.0804110105 (2008).

35 Santoro, R. *et al.* Encoding of natural sounds at multiple spectral and temporal resolutions in the human auditory cortex. *PLoS Comput Biol* **10**, e1003412, doi:10.1371/journal.pcbi.1003412 (2014).

36 Cai, Y., Hofstetter, S., van der Zwaag, W., Zuiderbaan, W. & Dumoulin, S. O. Individualized cognitive neuroscience needs 7T: Comparing numerosity maps at 3T and 7T MRI. *Neuroimage* **237**, 118184, doi:10.1016/j.neuroimage.2021.118184 (2021).

37 Vu, A. T. *et al.* Tradeoffs in pushing the spatial resolution of fMRI for the 7T Human Connectome Project. *Neuroimage* **154**, 23-32, doi:10.1016/j.neuroimage.2016.11.049 (2017).

38 Insel, T. R., Landis, S. C. & Collins, F. S. Research priorities. The NIH BRAIN Initiative. *Science* **340**, 687-688, doi:10.1126/science.1239276 (2013).

39 Zimmermann, J. *et al.* Mapping the organization of axis of motion selective features in human area MT using high-field fMRI. *PLoS One* **6**, e28716, doi:10.1371/journal.pone.0028716 (2011).

40 Park, S. H. *et al.* Functional Subpopulations of Neurons in a Macaque Face Patch Revealed by Single-Unit fMRI Mapping. *Neuron* **95**, 971-981 e975, doi:10.1016/j.neuron.2017.07.014 (2017).

41 *BRAIN 2025: A Scientific Vision (BRAIN 1.0)*, <https://braininitiative.nih.gov/sites/default/files/pdfs/brain2025_508c.pdf> (2014).

42 Jorgenson, L. A. *et al.* The BRAIN Initiative: developing technology to catalyse neuroscience discovery. *Philos Trans R Soc Lond B Biol Sci* **370**, doi:10.1098/rstb.2014.0164 (2015).

43 *BRAIN Initiave 2.0: From Cells to Circuits, Toward Cures (BRAIN 2.0)*, <https://braininitiative.nih.gov/sites/default/files/images/brain_2.0_6-6-19-final_revised10302019_508c.pdf> (2019).

44 Eisenstein, M. Pushing the limits of MRI brain imaging. *Nature Methods* **21**, 1975-1979, doi:10.1038/s41592-024-02489-y (2024).

45 Nowogrodzki, J. The world’s strongest MRI machines are pushing human imaging to new limits. *Nature* **563**, 24-26 (2018).

46 Ugurbil, K. *et al.* Progress in Imaging the Human Torso at the Ultrahigh Fields of 7 and 10.5 T. *Magn Reson Imaging Clin N Am* **29**, e1-e19, doi:10.1016/j.mric.2020.10.001 (2021).

47 Sadeghi-Tarakameh, A. *et al.* In vivo human head MRI at 10.5T: A radiofrequency safety study and preliminary imaging results. *Magn Reson Med* **84**, 484-496, doi:10.1002/mrm.28093 (2020).

48 He, X. *et al.* First in-vivo human imaging at 10.5T: Imaging the body at 447 MHz. *Magn Reson Med* **84**, 289-303, doi:10.1002/mrm.28131 (2020).

49 Grant, A. *et al.* 10.5 T MRI static field effects on human cognitive, vestibular, and physiological function. *Magn Reson Imaging* **73**, 163-176, doi:10.1016/j.mri.2020.08.004 (2020).

50 Schmidt, S. *et al.* Improved (1) H body imaging at 10.5 T: Validation and VOP-enabled imaging in vivo with a 16-channel transceiver dipole array. *Magn Reson Med* **91**, 513-529, doi:10.1002/mrm.29866 (2024).

51 Tkac, I. *et al.* Long-term behavioral effects observed in mice chronically exposed to static ultra-high magnetic fields. *Magn Reson Med* **86**, 1544-1559, doi:10.1002/mrm.28799 (2021).

52 Blamire, A. M. *et al.* Dynamic mapping of the human visual cortex by high-speed magnetic resonance imaging. *Proc Natl Acad Sci U S A* **89**, 11069-11073, doi:10.1073/pnas.89.22.11069 (1992).

53 Vizioli, L. *et al.* Lowering the thermal noise barrier in functional brain mapping with magnetic resonance imaging. *Nat Commun* **12**, 5181, doi:10.1038/s41467-021-25431-8 (2021).

54 Lagore, R. L. *et al.* A 128 Receive array with enhanced SNR Performance for 10.5 Tesla Brain Imaging. *bioRxiv*, doi:10.1101/2024.10.20.619294 (2024).

55 Cuppen, J. & van Est, A. Reducing MR imaging time by one-sided reconstruction. *Magn Reson Imaging* **5**, 526-527, doi:https://doi.org/10.1016/0730-725X(87)90402-4 (1987).

56 Cox, R. W., Chen, G., Glen, D. R., Reynolds, R. C. & Taylor, P. A. FMRI Clustering in AFNI: False-Positive Rates Redux. *Brain Connect* **7**, 152-171, doi:10.1089/brain.2016.0475 (2017).

57 Gulban, O. F. *et al.* Mesoscopic in vivo human T(2)(*) dataset acquired using quantitative MRI at 7 Tesla. *Neuroimage* **264**, 119733, doi:10.1016/j.neuroimage.2022.119733 (2022).

58 Moeller, S. *et al.* Multiband multislice GE-EPI at 7 tesla, with 16-fold acceleration using partial parallel imaging with application to high spatial and temporal whole-brain fMRI. *Magn Reson Med* **63**, 1144-1153, doi:10.1002/mrm.22361 (2010).

59 Ugurbil, K. *et al.* Pushing spatial and temporal resolution for functional and diffusion MRI in the Human Connectome Project. *Neuroimage* **80**, 80-104, doi:10.1016/j.neuroimage.2013.05.012 (2013).

60 Setsompop, K. *et al.* Blipped-controlled aliasing in parallel imaging for simultaneous multislice echo planar imaging with reduced g-factor penalty. *Magn Reson Med* **67**, 1210-1224, doi:10.1002/mrm.23097 (2012).

61 Marques, J. P. *et al.* MP2RAGE, a self bias-field corrected sequence for improved segmentation and T1-mapping at high field. *Neuroimage* **49**, 1271-1281, doi:10.1016/j.neuroimage.2009.10.002 (2010).

62 Schreiber, S., Northall, A., Weber, M., Vielhaber, S. & Kuehn, E. Topographical layer imaging as a tool to track neurodegenerative disease spread in M1. *Nat Rev Neurosci* **22**, 68-69, doi:10.1038/s41583-020-00404-w (2021).

63 McColgan, P., Joubert, J., Tabrizi, S. J. & Rees, G. The human motor cortex microcircuit: insights for neurodegenerative disease. *Nat Rev Neurosci* **21**, 401-415, doi:10.1038/s41583-020-0315-1 (2020).

64 Triantafyllou, C. *et al.* Comparison of physiological noise at 1.5 T, 3 T and 7 T and optimization of fMRI acquisition parameters. *Neuroimage* **26**, 243-250, doi:10.1016/j.neuroimage.2005.01.007 (2005).

65 Triantafyllou, C., Polimeni, J. R. & Wald, L. L. Physiological noise and signal-to-noise ratio in fMRI with multi-channel array coils. *Neuroimage* **55**, 597-606, doi:10.1016/j.neuroimage.2010.11.084 (2011).

66 Feinberg, D. A. *et al.* Next-generation MRI scanner designed for ultra-high-resolution human brain imaging at 7 Tesla. *Nat Methods* **20**, 2048-2057, doi:10.1038/s41592-023-02068-7 (2023).

67 Pruessmann, K. P., Weiger, M., Scheidegger, M. B. & Boesiger, P. SENSE: sensitivity encoding for fast MRI. *Magn Reson Med* **42**, 952-962 (1999).

68 Wiesinger, F. *et al.* Parallel imaging performance as a function of field strength--an experimental investigation using electrodynamic scaling. *Magn Reson Med* **52**, 953-964, doi:10.1002/mrm.20281 (2004).

69 Wiesinger, F. *et al.* Potential and feasibility of parallel MRI at high field. *NMR Biomed* **19**, 368-378, doi:10.1002/nbm.1050 (2006).

70 Ugurbil, K. *et al.* Brain imaging with improved acceleration and SNR at 7 Tesla obtained with 64-channel receive array. *Magn Reson Med* **82**, 495-509, doi:10.1002/mrm.27695 (2019).

71 Gruber, B. *et al.* A 128-channel receive array for cortical brain imaging at 7 T. *Magn Reson Med* **90**, 2592-2607, doi:10.1002/mrm.29798 (2023).

72 Harel, N., Lin, J., Moeller, S., Ugurbil, K. & Yacoub, E. Combined imaging-histological study of cortical laminar specificity of fMRI signals. *Neuroimage* **29**, 879-887, doi:10.1016/j.neuroimage.2005.08.016 (2006).

73 Kim, S. G. & Ugurbil, K. High-resolution functional magnetic resonance imaging of the animal brain. *Methods* **30**, 28-41 (2003).

74 Goense, J. B. & Logothetis, N. K. Laminar specificity in monkey V1 using high-resolution SE-fMRI. *Magn Reson Imaging* **24**, 381-392, doi:10.1016/j.mri.2005.12.032 (2006).

75 Huber, L. *et al.* High-Resolution CBV-fMRI Allows Mapping of Laminar Activity and Connectivity of Cortical Input and Output in Human M1. *Neuron* **96**, 1253-1263 e1257, doi:10.1016/j.neuron.2017.11.005 (2017).

76 Moerel, M. *et al.* Sensitivity and specificity considerations for fMRI encoding, decoding, and mapping of auditory cortex at ultra-high field. *Neuroimage* **164**, 18-31, doi:10.1016/j.neuroimage.2017.03.063 (2018).

77 Yacoub, E. *et al.* Spin-echo fMRI in humans using high spatial resolutions and high magnetic fields. *Magn Reson Med* **49**, 655-664, doi:10.1002/mrm.10433 (2003).

78 Yacoub, E., Ugurbil, K. & Harel, N. Detection of orientation specific activation zones in human V1 using fMRI. *Proc. Intl. Soc. Mag. Reson. Med.*, 892 (2006).

79 Yacoub, E., Shmuel, A., Logothetis, N. & Ugurbil, K. Robust detection of ocular dominance columns in humans using Hahn Spin Echo BOLD functional MRI at 7 Tesla. *Neuroimage* **37**, 1161-1177, doi:10.1016/j.neuroimage.2007.05.020 (2007).

80 Huber, L. *et al.* Techniques for blood volume fMRI with VASO: From low-resolution mapping towards sub-millimeter layer-dependent applications. *Neuroimage* **164**, 131-143, doi:10.1016/j.neuroimage.2016.11.039 (2018).

81 Ugurbil, K. Ultrahigh Field and Ultrahigh Resolution fMRI. *Curr Opin Biomed Eng* **18**, doi:10.1016/j.cobme.2021.100288 (2021).

82 Duong, T. Q. *et al.* Microvascular BOLD contribution at 4 and 7 T in the human brain: gradient-echo and spin-echo fMRI with suppression of blood effects. *Magn Reson Med* **49**, 1019-1027, doi:10.1002/mrm.10472 (2003).

83 Sotiropoulos, S. N. *et al.* Advances in diffusion MRI acquisition and processing in the Human Connectome Project. *Neuroimage* **80**, 125-143, doi:10.1016/j.neuroimage.2013.05.057 (2013).

84 Demirel, O. B. *et al.* 20-fold Accelerated 7T fMRI Using Referenceless Self-Supervised Deep Learning Reconstruction. *Annu Int Conf IEEE Eng Med Biol Soc* **2021**, 3765-3769, doi:10.1109/EMBC46164.2021.9631107 (2021).

85 Kilic, T. *et al.* Unsupervised deep learning with convolutional neural networks for static parallel transmit design: A retrospective study. *Magn Reson Med*, doi:10.1002/mrm.30014 (2024).

86 Stigliani, A., Weiner, K. S. & Grill-Spector, K. Temporal Processing Capacity in High-Level Visual Cortex Is Domain Specific. *J Neurosci* **35**, 12412-12424, doi:10.1523/JNEUROSCI.4822-14.2015 (2015).

87 Bekinschtein, T. A. *et al.* Neural signature of the conscious processing of auditory regularities. *Proc Natl Acad Sci U S A* **106**, 1672-1677, doi:10.1073/pnas.0809667106 (2009).

88 Waks, M. *et al.* RF coil design strategies for improving SNR at the ultrahigh magnetic field of 10.5 Tesla. *bioRxiv*, doi:10.1101/2024.05.23.595628 (2024).

89 Huber, L. R. *et al.* LayNii: A software suite for layer-fMRI. *Neuroimage* **237**, 118091, doi:10.1016/j.neuroimage.2021.118091 (2021).

90 Cox, R. W. AFNI: software for analysis and visualization of functional magnetic resonance neuroimages. *Comput Biomed Res* **29**, 162-173, doi:10.1006/cbmr.1996.0014 (1996).

91 Moeller, S. *et al.* NOise reduction with DIstribution Corrected (NORDIC) PCA in dMRI with complex-valued parameter-free locally low-rank processing. *Neuroimage* **226**, 117539, doi:10.1016/j.neuroimage.2020.117539 (2021).

SUPPLEMENTARY MATERIAL

i) The resolution effect on large vein contributions to GRE BOLD fMRI

If one considers an infinite cylinder as an approximation for a blood vessel with magnetic susceptibility difference $\Delta\chi$ relative to its surrounding, the applied magnetic field of B_0 will be perturbed and deviate from it outside the cylinder.[1-3] This perturbation, expressed as $\Delta\omega_B^{out}$ in rad/s, relative to the magnetic field distant from the cylinder, ω_0, will be given by the equation

$$\Delta\omega_B^{out} = 2\pi\Delta\chi\omega_0(r_b/r)^2 sin^2(\theta)cos(2\phi) \quad (1)$$

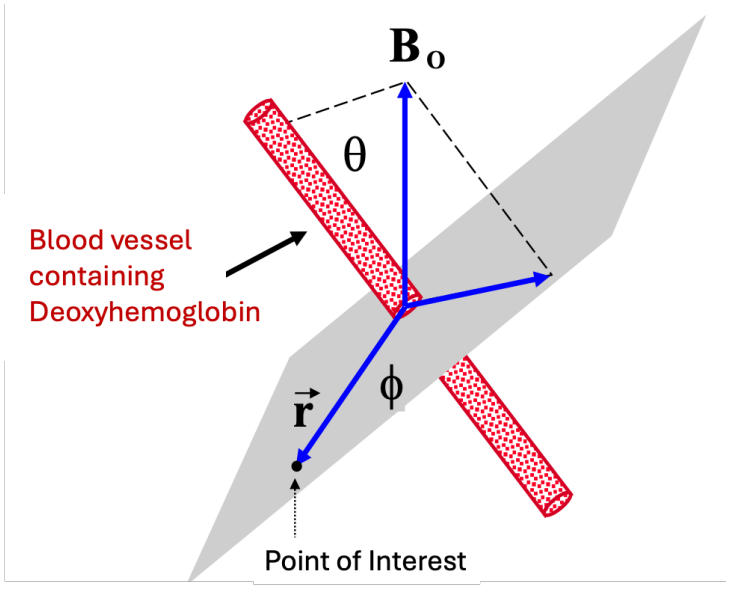

SUPPLEMENTARY FIGURE S1: Definition of the variables given in Eq.1

In the above equations, ω_0 is B_0 expressed as Larmor frequency in rad/s (i.e. $\omega_0 = \gamma B_0$ where and γ is the gyromagnetic ratio) θ is the angle between the applied magnetic field B_0 direction and the cylinder axis in a plane that contains them both, r_b is the cylinder radius, r is the distance between the point of interest and the center of the cylinder cross-section in the plane normal to the cylinder, and ϕ is the angle between this vector ($\vec{r}$) and the component of B_0 in this plane (Figure S1). The BOLD effect originates from the intra-voxel inhomogeneity caused by $\Delta\omega_B^{out}$ outside the deoxyhemoglobin containing blood vessels. BOLD fMRI signals arise when this intra-voxel inhomogeneity is altered due to small changes in $\Delta\chi$ and/or r_b induced by alterations in neuronal

activity. Therefore, the mechanistically critical phenomenon in extravascular BOLD effect is the intra-voxel inhomogeneity caused by the inhomogeneous $\Delta\omega_B^{out}$.

Lumping all the terms in Eq. 1 other than (r_b/r) into a function designated as $K(\theta, \phi, \Delta\chi)$, we can express $\Delta\omega_B^{out}$ as

$$\Delta\omega_B^{out}(\vec{r}) = K(\theta, \phi, \Delta\chi) \cdot (r_b/r)^2 \tag{2}$$

If we consider the problem only in one-dimension along the vector $(\vec{r})$, limiting ourselves for convenience to a one-dimensional imaging so to speak, the gradient of the magnetic field with respect to r will be given by the derivative of Eq. 2,

$$\frac{\partial\Delta\omega_B^{out}}{\partial r} = -2K(\theta, \phi, \Delta\chi) \cdot \left(\frac{r_b^2}{r^3}\right) \tag{3}$$

Across a one-dimensional voxel of dimension δr then, for small δr, the magnetic field variation across the voxel (i.e. intra-voxel magnetic field inhomogeneity) will be given by:

$$\delta r \cdot \frac{\partial\Delta\omega_B^{out}}{\partial r} = -2K(\theta, \phi, \Delta\chi) \cdot \delta r \left(\frac{r_b^2}{r^3}\right) = -2K(\theta, \phi, \Delta\chi) \cdot \left(\frac{\delta r}{r_b}\right) \cdot \left(\frac{r_b}{r}\right)^3 \tag{4}$$

This intra-voxel magnetic field variation will induce intravoxel-dephasing during a delay TE in the GRE BOLD fMRI acquisition, reducing the amplitude of the signal detected for this voxel. This is the BOLD effect. Alterations in neuronal activity will induce changes in the intra-voxel dephasing and hence in the signal amplitude of the voxel, giving rise to the functional signals in fMRI.

The variation of $\Delta\omega_B^{out}$ within a voxel of dimension δr at the surface of the blood vessel where $r = r_b$ will be

$$\delta r \cdot \frac{\partial\Delta\omega_B^{out}}{\partial r} = -2K(\theta, \phi, \Delta\chi) \cdot \left(\frac{\delta r}{r_b}\right) \qquad (r = r_b) \tag{5}$$

Thus, the gradient of the magnetic field outside the blood vessel is steepest at/near the luminal boundaries of the blood vessel where $r = r_b$, and will decrease from that value as the cube power of (r_b/r) with increasing distance away from the blood vessel. As the resolution gets higher (i.e. δr gets smaller) relative to the blood vessel radius, in the limit $(\delta r/r_b) \ll 1$, the intra-

voxel variation of the magnetic field for all voxels outside the cylinder will altogether disappear. Hence the signal amplitude decrease during TE (i.e. the extravascular BOLD effect manifested as an amplitude modulation) will also vanish beyond detection limits. Note that extravascular perturbations of the magnetic field outside the deoxyhemoglobin containing blood vessel given by Eq.1 stills exist and can be detected as a phase variation over spatial coordinates but will not be detected in a standard GRE BOLD fMRI experiment which looks at signal amplitude changes.

For blood vessels that do not fully satisfy this condition (e.g. $\delta r \sim r_b$), the BOLD effect will persist near the blood vessel boundary where the gradient is large. However, with increasing separation from the blood vessel, the intra-voxel magnetic field variation, given by Eq. 4, will rapidly decrease according to $(r_b/r)^3$, vanishing when $\delta r(r_b^2/r^3) \ll 1$. In other words, as $(\delta d/r_b)$ gets smaller, the extravascular BOLD effect (detected as signal amplitude associated with a voxel), starts progressively shrinking towards the blood vessel and appears in close proximity to the blood vessel boundary where the gradient is steepest. This is what is observed in Figure 5c.

The condition $(\delta r/r_b) \lesssim 1$ can be satisfied for different size draining veins at submillimeter spatial resolutions. But it will be far from being satisfied for capillaries (diameter[4] ~5.1±0.84 μm) and postcapillary venules (few tens of microns in diameter). Hence, as the spatial resolution increases, the microvascular BOLD effect remains unaffected while the large vein contributions decrease, leading to increased domination of the microvascular contribution at the very high magnetic fields.

There is of course also an intravascular BOLD effect. However, the T2 of deoxyhemoglobin containing blood decreases rapidly with increasing magnetic fields so that at fields ≳7 Tesla, at TEs that approximate the tissue T2, as employed in GRE BOLD fMRI, the blood signal disappears[5]. At lower magnetic fields, the intravascular BOLD effect remains significant (e.g. at 3 Tesla it was estimated to be ~50% of the BOLD signal[6]) and can be a source of draining vein signals. Thus, the suppression of draining-veins through high resolutions requires

the high magnetic fields because of the high SNR needs of high-resolution imaging but also for eliminating the intravascular BOLD effect.

The resolution effect discussed above can also be conceptualized using simple GRE images of a brain slice (Supplementary Figure S2) where signal intensity dropouts occur near the air-filled cavities in the frontal regions because of magnetic field inhomogeneities. Analogous to the EV BOLD effect this intensity dropout is induced by the susceptibility difference between brain tissue and air. At high enough resolutions, as the voxel dimensions get smaller compared to the distances over which magnetic fields vary due to this susceptibility difference, the intra-voxel signal variation becomes smaller and the signal drop-outs disappear. This is illustrated in Figure S2 with an image acquired with 5 mm slice thickness versus a 1 mm slice thickness.

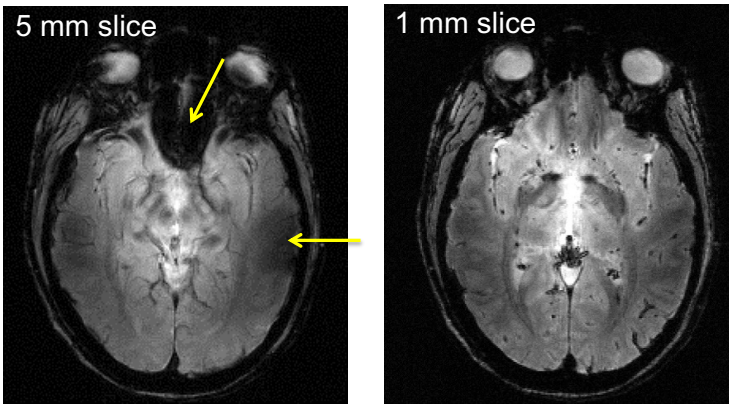

SUPPLEMENTARY FIGURE S2: Gradient recalled echo images in the human brain of a slice through a region near nasal cavities and sinuses. The left panel has a lower resolution due to 5 mm slice thickness. Total signal dropout is observed in the frontal areas and in addition, signal intensity reduction (hence darker image intensity) is observed near the ears (yellow arrows). These are well known effects associated with the presence of magnetic field gradients near the air-filled cavities in the human head. Reducing the voxel volume by cutting down the slice thickness eliminates the signal dropout in the frontal areas and improves image intensity near the ears.

ii) 0.65 mm isotropic Functional Imaging with Auditory Stimulation with Standard Vendor reconstruction

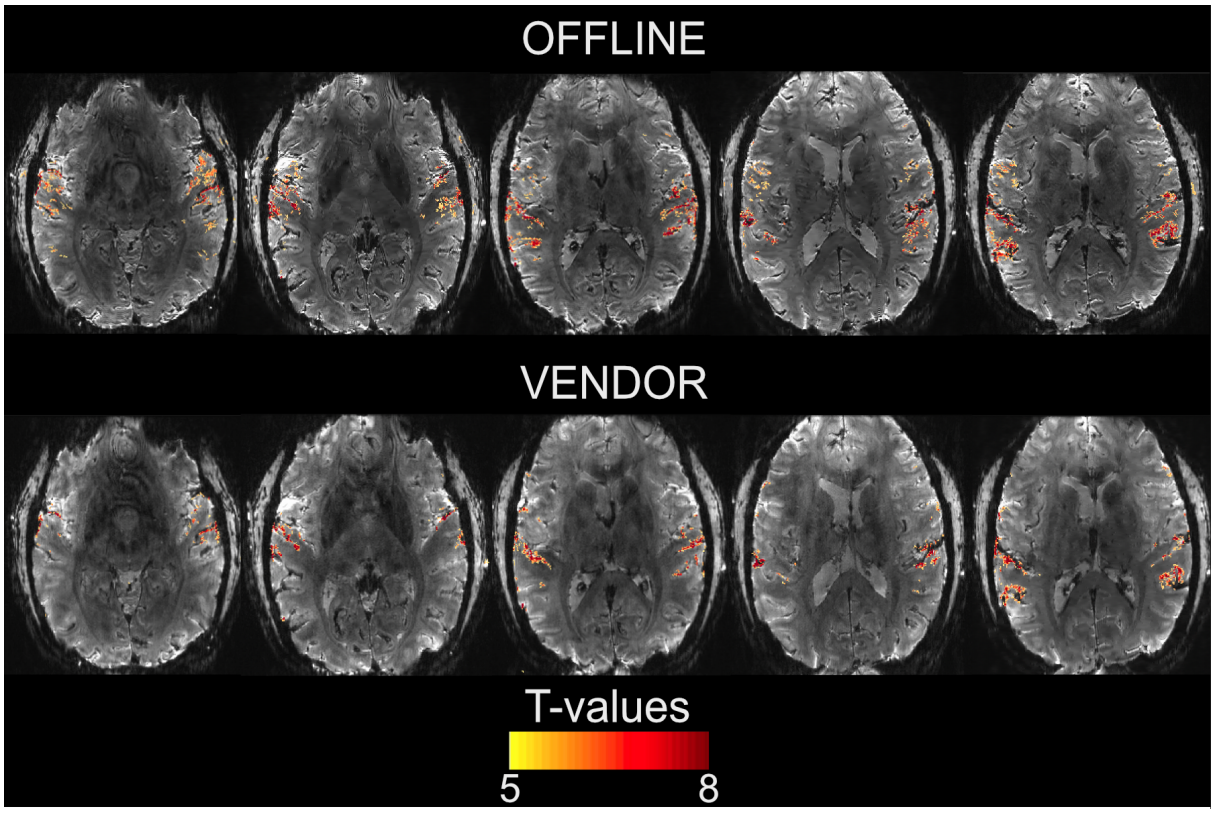

SUPPLEMENTARY FIGURE S3: Example of the highest resolution achieved for auditory functional mapping in humans (i.e. 0.65mm isotropic). We show functional maps for the t-contrast Sounds > 0 for 6 concatenated runs superimposed on exemplar slices of single epi images for our tailored offline (top) and vendor reconstructed images. While, as expected, our offline reconstruction leads to superior functional mapping, the SNR gains afforded by 10.5T

Images above display functional maps of auditory stimulation obtained at 0.65 mm isotropic resolution and reconstruction using vendor supplied routines based on Zero filling the k-space for the unacquired data in partial Fourier.

REFERENCES for the SUPPLEMENTARY MATERIAL

1 Springer, C. S. & Xu, Y. in *New Developments in Contrast Agent Research* (eds P.A. Rink & R.N. Muller) 13-25 (European Magnetic Resonance Forum, 1991).

2 Ogawa, S., Menon, R. S., Tank, D. W., Kim, S. G., Merkle, H., Ellermann, J. M. & Ugurbil, K. Functional brain mapping by blood oxygenation level-dependent contrast magnetic resonance imaging. A comparison of signal characteristics with a biophysical model. (1993) *Biophys J* **64**, 803-812, **doi**:10.1016/S0006-3495(93)81441-3.

3 Ugurbil, K., Adriany, G., Andersen, P., Chen, W., Gruetter, R., Hu, X., Merkle, H., Kim, D. S., Kim, S. G., Strupp, J., Zhu, X. H. & Ogawa, S. Magnetic resonance studies of brain function and neurochemistry. (2000) *Annu Rev Biomed Eng* **2**, 633-660.

4 Pawlik, G., Rackl, A. & Bing, R. J. Quantitative capillary topography and blood flow in the cerebral cortex of cats: an in vivo microscopic study. (1981) *Brain Res* **208**, 35-58.

5 Duong, T. Q., Yacoub, E., Adriany, G., Hu, X., Ugurbil, K. & Kim, S. G. Microvascular BOLD contribution at 4 and 7 T in the human brain: gradient-echo and spin-echo fMRI with suppression of blood effects. (2003) *Magn Reson Med* **49**, 1019-1027, **doi**:10.1002/mrm.10472.

6 Jochimsen, T. H., Norris, D. G., Mildner, T. & Moller, H. E. Quantifying the intra- and extravascular contributions to spin-echo fMRI at 3 T. (2004) *Magn Reson Med* **52**, 724-732.